RSMAS TECHNICAL REPORT 95-007

VHF RADAR MEASUREMENTS OF OCEAN SURFACE CURRENTS

FROM A MOVING SHIP

by

Nicholas J. Peters and Richard A. Skop

Division of Applied Marine Physics
Rosenstiel School of Marine and Atmospheric Science
University of Miami
Miami, FL 33149

19960213 020

August 1995

DTIC QUALITY INSPECTED 4

REPORT DOCUMENTATION PAGE

1. AGENCY USE ONLY (Leave blank)	2. REPORT DATE August 1995	3. REPORT TYPE AND DATES COVERED

4. TITLE AND SUBTITLE
VHF RADAR MEASUREMENTS OF OCEAN SURFACE CURRENTS FROM A MOVING SHIP

5. FUNDING NUMBERS
N00014-93-1-G900
N00014-95-1-G905

6. AUTHOR(S)
Nicholas J. Peters and Richard A. Skop

7. PERFORMING ORGANIZATION NAME(S) AND ADDRESS(ES)
Division of Applied Marine Physics
Rosenstiel School of Marine & Atmospheric Science
University of Miami, 4600 Rickenbacker Causeway
Miami, FL 33149

8. PERFORMING ORGANIZATION REPORT NUMBER
RSMAS Technical Report 95-007

9. SPONSORING/MONITORING AGENCY NAME(S) AND ADDRESS(ES)
Naval Research Laboratory (SSC)   Office of Naval Research
Code 7410   Remote Sensing Program
Stennis Space Center, MS 39529   800 N. Quincy Street
                                       Arlington, VA 22217

10. SPONSORING/MONITORING AGENCY REPORT NUMBER
CR/7410--95-0040

11. SUPPLEMENTARY NOTES

12a. DISTRIBUTION/AVAILABILITY STATEMENT

Approved for public release. Distribution unlimited.

12b. DISTRIBUTION CODE

13. ABSTRACT (Maximum 200 words)

Shore-based, high frequency (HF) and very high frequency (VHF) radar systems for measuring ocean surface currents have been well detailed in the literature. The use of these systems has been limited to coastal ocean applications since both of the required radar sites must be positioned ashore. To relieve the geometric constraints imposed by two shore sites and allow coverage of more coastal areas, necessitates at least one sea-based system (Skop et al., 1994). Reducing the number of required sites to one increases the ocean area that can be measured. The feasibility of using a single, VHF radar system based on a moving ship for both near shore and deep water area coverage is the subject of this report.

In December 1993 and July 1994 a near shore, ship-based data set was taken off the east coast of Key Biscayne, Florida, with overlapping coverage by a shore-based site. The July 1994 experiment also saw deep water data sets acquired as the ship described a square pattern to obtain overlapping grid coverage from the ship itself. The measurement and reduction of ship-induced contamination in the returned Doppler spectra are detailed. By combining ship and shore radial data, two vector current maps off north and south Key Biscayne are obtained. Using the same methodology, the vectorization of the deep water radials produces two more vector current maps from one transmit-receive ship-based site.

The deep water surface current maps are dominated by the high speed, northerly flowing Florida Current and are quite accurate. The Key Biscayne surface current maps are less accurate, being dominated by pseudo-currents that are introduced through GPS errors in ship position. These GPS errors lead to inaccurate calculations of the ship velocity and, hence, to inaccurate removal of the ship-induced Doppler currents from the measured currents. Two methods of correcting for these GPS errors are discussed. The implementation of both methods would enable small currents to be mapped with a high degree of confidence from a single, moving ship.

14. SUBJECT TERMS
VHF Radar, Surface Currents, Coastal Currents, Radar Backscatter, Remote Sensing

15. NUMBER OF PAGES
60

16. PRICE CODE

17. SECURITY CLASSIFICATION OF REPORT	18. SECURITY CLASSIFICATION OF THIS PAGE	19. SECURITY CLASSIFICATION OF ABSTRACT	20. LIMITATION OF ABSTRACT
Unclassified	Unclassified	Unclassified	

RSMAS TECHNICAL REPORT 95-007

VHF RADAR MEASUREMENTS OF OCEAN SURFACE CURRENTS

FROM A MOVING SHIP

by

Nicholas J. Peters and Richard A. Skop

Division of Applied Marine Physics
Rosenstiel School of Marine and Atmospheric Science
University of Miami
Miami, FL 33149

August 1995

CONTENTS

INTRODUCTION

The utilization of HF radar for the observation of ocean parameters was first realized when Crombie (1955) correctly deduced the scattering mechanism which accounted for the two strong peaks appearing above and below the carrier frequency in the Doppler spectrum. These Bragg peaks are the result of the superposition of the reflected radiation at grazing incidence by ocean waves moving directly towards or away from the radar and having a wavelength of half the wavelength of the transmitted signal.

The difference of the received Bragg scattered frequency peak from its expected value is due to the non-zero speed of the medium in which the reflecting waves are moving, i.e. the ocean surface currents. Thus, a radial current can be directly deduced from the spectral return. Vectorization of the radial currents from two radar sites with overlapping coverage leads to current speed and direction.

This Doppler radar technique has been used successfully for many years for shore-based measurements of coastal ocean circulation (Barrick, 1972; Stewart and Joy, 1974; Schott et al., 1986; Prandle, 1987; Shay et al., 1993). The system currently employed by the University of Miami is the Ocean Surface Current Radar (OSCR), developed by Marex. This is a pulsed radar using a 4 element Yagi transmit antenna limiting beamwidth to a 90° arc and minimizing backward signals. The receive antenna is a multi-element linear array consisting of up to 32 elements for the VHF mode of operation (49.95 MHz). The system has a spatial resolution of 250 m and maximum range of 11 km. The Bragg resonant wavelength is 3 m. The phased receive array allows angular resolution of the received signals. Accurate timing allows distance resolution. From the range and bearing capabilities, a grid of up to 700 data points is generated. Each one of these discrete bins has a vector current associated with it.

In December 1993, one transmit and receive site was established on the RV COLUMBUS ISELIN, a 50 m University of Miami research vessel, which was subsequently four point anchored off Key Biscayne, Florida, and positioned to form the grid coverage with a shore site

1

on Key Biscayne. Some cells were located co-linearly to facilitate comparisons of the returned spectra. Variations of the ship-based Doppler spectrum expected due to the ship motions and superstructure interference could then be characterized. The ship motions were recorded with a six channel accelerometer system (Skop et al., 1994).

In the latter part of the December experiment, the ship transited at a speed of 1 m/s during the transmit and receive cycles to examine the possibility of generating the vector current maps from a moving platform. The moving ship experiment was repeated in July 1994 to obtain additional data. During the July trials, the ship also transected a square pattern offshore of Key Biscayne and within the Florida Current. The send and receive cycles occurred at the central position of each of the square sides. The objective here was to place a set of overlapping deep water grids of the OSCR footprint and, again, to examine the possibility of generating vector current maps from a single, moving platform. The reduction and analysis of the moving ship data are the subject of this report.

The results demonstrate the capability of a ship-based OSCR system to obtain Doppler spectra of sufficient integrity for subsequent evaluation of ocean surface currents. The overriding inaccuracies in the calculated currents were uncertainties in the ship speed due to GPS errors in the determination of ship position. Two methods of correcting for these inaccuracies are discussed. Greater precision in the GPS recordings can be obtained by using differential or military GPS systems. Algorithms can also be derived to minimize the pseudo-circulation pattern due to GPS errors. The implementation of both methods would enable small currents to be mapped with a high degree of confidence from a single, moving ship.

The ability to measure ocean surface currents from a single, moving platform has numerous applications. Examples are support of Naval amphibious operations, tracking of oil and other toxic spills, and mapping of dynamic ocean features.

OCEAN SURFACE CURRENT RADAR

Bragg Backscatter

The principle behind HF radar as a remote sensing tool for ocean surface parameters lies in the exact predictability of the returning signal. Ocean waves are dispersive with frequency proportional to the square root of the wave number. In deep water, gravity waves travel at a phase velocity, C_p, proportional to the square root of the wavelength λ, such that

$$C_p = \sqrt{\frac{g\lambda}{2\pi}} \tag{1}$$

where $g = 9.81$ m/s^2 is the acceleration due to gravity. Ocean wave trains can be assumed to act like a series of diffraction gratings with an unique orientation and spacing providing the returning Doppler spectrum with two resonant peaks (Crombie, 1955). For ground wave propagation (i.e. reflection near grazing incidence), this spacing is precisely half that of the radar wavelength. As these resonant waves can be uniquely described in terms of their associated velocity, shifts from the expected Bragg frequency are the direct result of ocean currents.

Transmission Parameters

The OSCR radio transmission is a pulsed HF or VHF signal. For the deployments of the system discussed in this report, the VHF mode was chosen. The 250 m by 250 m resolution in this mode allows detailed surface features to be resolved. The pulse repetition interval (PRI), defined as the time between successive transmit cycles, is in this operating approach

$$PRI = 80 \ \mu s \tag{2}$$

The pulse length (duration) δ is

$$\delta = 1.667 \ \mu s \tag{3}$$

The maximum range $R_{\max}$ of the system is calculated as

$$R_{\max} = \frac{c}{2}(PRI - \delta) \tag{4}$$

where $c = 2.997 \times 10^8$ m/s is the speed of light. The range resolution ΔR in the VHF mode is

$$\Delta R = \frac{c\delta}{2} \qquad (5)$$

Equations (4) and (5) provide

$$\Delta R = 250 \ m$$

and

$$R_{max} = 11.75 \ km$$

In fact, the range is about 11 km due to constraints of the hardware. However, the resolution is correct if the changes in area due to increased radial distance from the transmit antenna are ignored. This modification is unnecessary in the limited distances considered for the VHF array.

Receive Array Parameters

The multi-element linear receive array at the shore site consisted of 16 omni-directional passive whip antennas with 3 m (i.e., half transmit wavelength) separation. The ship-based receive array consisted of 12 antennas due to space restrictions.

In the VHF (50 MHz) mode, each pulse contains 83.35 cycles (50 MHz * 1.667 μs) of the carrier frequency. The return echo of the first pulse is received by the first antenna only. The first return is demodulated against the carrier frequency sequentially into in-phase I and out-of-phase Q components 42 cycles at a time. Range gating of the return provides I/Q values for 41 distinct range bins. The second pulse is received by the second antenna; this continues sequentially for all elements. In actuality this is done for 32 elements, regardless of the actual number used, with non-existent elements ignored in the data processing. This sequence of send-receive cycles takes approximately 2.56 ms. The entire stage is repeated 32 times. The resultant I/Q's for each individual antenna are summed to increase the signal to noise ratio. Total time for the final summed I/Q's to be recorded is just under a third of a second.

These summed values are then transferred to the beamforming software as the summing cycle is re-initiated. In the beamformer, phased summation produces I/Q values for each of the 700 cells for the first cycle. The entire process is repeated 896 times and the results for each

4

repetition are recorded separately. The 896 repetitions take just under five minutes to complete. The data array I/Q is transformed into the frequency domain using a Fast Fourier Transform (FFT), first on the first 512 time points, and then on the last 512 time points. The two FFT's are then summed frequency by frequency to produce the final Fourier power spectrum of 512 values. The overlapping spectral estimates increase the signal to noise ratio as the signal is summed in phase, and the noise is summed with random phase. A gain of 3 dB is achieved. From here the software moves into the peak picking routine.

Peak Picking and Current Extraction

The returned spectra of the Fourier power spectrum contains 512 frequency points spanning from -1.52 to +1.52 Hz. A five-point running average is used to smooth the data, From this smoothed spectrum, the ten largest peaks are selected. For each peak, the corresponding theoretical position of it's Bragg pair is calculated. The expected frequency separation is 2 *FBG* where *FBG* is the nominal Doppler frequency and is given by

$$FBG = \sqrt{\frac{g\, f_T}{\pi\, c}} \tag{6}$$

where f_T is the radar frequency. For the VHF mode, *FBG* = 0.7214 Hz. The closest paired peaks are then selected, and their frequency offset, *FF*, is calculated by

$$FF = \frac{((FP(R)+FBG)*PP(R)+(FP(A)-FBG)*PP(A))}{(PP(R)+PP(A))} \tag{7}$$

Here $FP(R)$ and $FP(A)$ are the Doppler frequencies of the receding and advancing peaks, and $PP(R)$ and $PP(A)$ are their spectral powers. This approach weights the resulting calculated frequency shift towards the stronger peak chosen. The radial velocity R_V is found from this frequency offset. The radial velocity, *DTV* in m/s per unit Doppler shift (i.e., one frequency bin) is

$$DTV = 0.50 \times \frac{c}{f_T} \tag{8}$$

and the actual radial velocity is the product of the frequency offset and *DTV*, or

$$R_V = FF*DTV \tag{9}$$

The sign of the calculated frequency offset corresponds to the direction of the measured

5
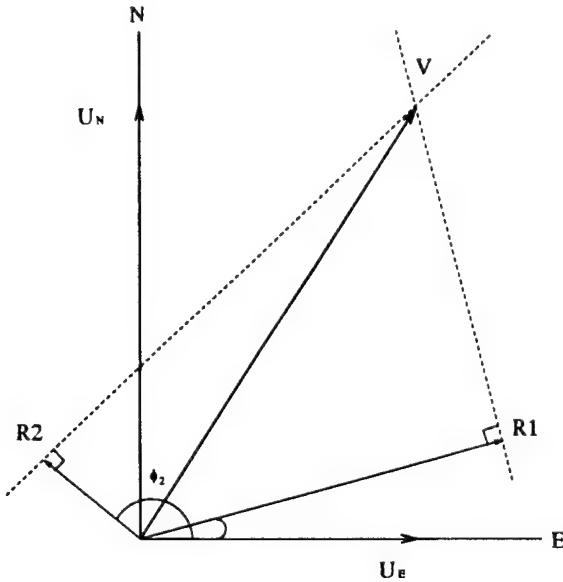
Figure 1. Vectorization of the radials.

radial current. A positive shift, for example, represents an increased frequency due to the Doppler effect and indicates a current moving towards the receive array. A negative shift implies a current moving away from the receive array.

The vector current is calculated by combining the two radials into a two dimensional current based on the geometric constraints of the array configuration. For each of the grid points, the bearing ϕ_1 of the radial velocity R_1 and the bearing ϕ_2 of the radial velocity R_2 are calculated. The bearings are referenced counterclockwise from east. The bearings and radials are shown in Figure 1. Both radials are taken as positive; the bearing of the radial now determining whether the flow is towards or away from its associated receive array. The northerly and easterly components of the flow are denoted by U_N and U_E, respectively. The equations of the lines perpendicular to the tips of R_1 and R_2 are found from Figure 1 as

$$U_N = -\frac{U_E}{\tan\phi_1} + \frac{R_1}{\sin\phi_1} \tag{10}$$

$$U_N = -\frac{U_E}{\tan\phi_2} + \frac{R_2}{\sin\phi_2} \tag{11}$$

6

The intersection of these two lines gives the specific values of U_N and U_E of the vector current as

$$U_E = \frac{R_1 \sin\phi_2 - R_2 \sin\phi_1}{\sin(\phi_2 - \phi_1)} \tag{12}$$

$$U_N = \frac{R_1 \cos\phi_2 - R_2 \cos\phi_1}{\sin(\phi_1 - \phi_2)} \tag{13}$$

The current components can be combined to determine the current magnitude as

$$V = \sqrt{U_E^2 + U_N^2} \tag{14}$$

and the direction of the current relative to east is calculated as

$$\arctan(U_N/U_E) \ if \ U_E \geq 0$$

$$\arctan(U_N/U_E) + 180^\circ \ if \ U_E < 0 \tag{15}$$

Based on Nyquist sampling theory (Brigham, 1974), the accuracy of the surface current determined by the OSCR system is ±2 cm/s in the VHF mode. The angular resolution is ±5°.

FACTORS AFFECTING THE SPECTRA RESULTING FROM SHIP MOTIONS

Ship-Induced Doppler

To evaluate the returned signal, the effect of the ship motion on the Doppler spectrum must be assessed. Consider the situation shown in Figure 2. The velocity of the source (transmit antenna) along the line-of-sight between the source and the target is given by

$$v = V_{SH} + V_S \cos(\omega t) \tag{16}$$

where V_{SH} is the steady velocity of the ship along the line-of-sight, V_S is the magnitude of the oscillations about V_{SH} and ω is the frequency of the oscillations. The velocity of the target (radial Bragg waves) towards the ship is given by

$$v = V_T \tag{17}$$

Finally, the velocity of the receiver (array antenna) is given by

$$v = V_{SH} + V_R \cos(\omega t) \tag{18}$$

where V_R is the magnitude of the oscillations of the receiver about V_{SH}.

The received signal is delayed in time from the source signal by the round trip travel time R_{TOT}/c. Here, R_{TOT} is the round trip travel distance from the source to the target to the receiver and is determined as

$$R_{TOT} = 2R_0 - 2(V_T + V_{SH})t - \frac{(V_S + V_R)}{\omega}\sin(\omega t) \tag{19}$$

where R_0 is the distance from the source (and receiver) to the target at time $t = 0$ (the start of a transmission pulse). The phase ψ of the received signal relative to the transmitted signal is then

$$\psi = -\frac{2\pi f_T R_{TOT}}{c} = 2\pi\left[\frac{(V_T + V_{SH})t}{\lambda} + \frac{(V_S + V_R)T}{4\pi\lambda}\sin\left(\frac{2\pi t}{T}\right)\right] \tag{20}$$

8

SOURCE

○

$v = V_{SH} + V_S \cos(\omega t)$

TARGET

○

- - - - - - - - - - - - - - ->
LINE-OF-SIGHT

<- - - - - - - -

RECEIVER

○

$v = V_T$

$v = V_{SH} + V_R \cos(\omega t)$
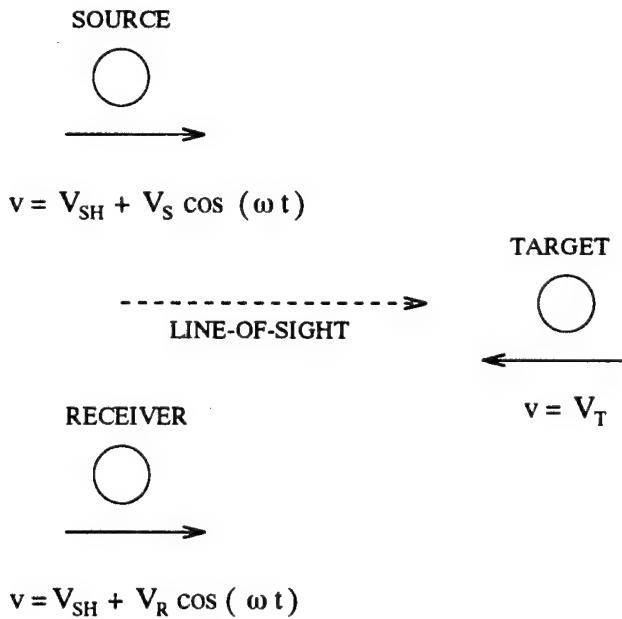
Figure 2. Schematic of source, target and receiver.

In writing equation (20), the constant phase due to the R_0 term in R_{TOT} has been suppressed as unimportant and the relation $\omega = 2\pi/T$ has been used where T is the period of oscillation of the ship. After frequency demodulation of the received signal against the transmitted signal, the modulation signal $Y(t)$ can be described as

$$Y(t) = A\cos\psi + B\sin\psi \qquad (21)$$

where A and B are amplitudes.

For the OSCR deployments, the boresite of the receive array was normal to the centerplane of the ship as sketched in Figure 3. The angle between the boresite and a cell located at some point R is denoted by θ. The unit vector $\hat{r}$ along θ is then

$$\hat{r} = \cos\theta\,\hat{\imath} + \sin\theta\,\hat{\jmath} \qquad (22)$$

where $\hat{\imath}$ and $\hat{\jmath}$ are unit vectors along the X and Y directions, respectively. Further, $\overline{U}$ denotes the steady motion of the ship along the Y axis and $\overline{V}$ denotes the steady motion along the X axis. The velocity at the source is then

$$\vec{V}_S = [\overline{V} + v'_s\cos(\omega t)]\,\hat{\imath} + [\overline{U} + u'_s\cos(\omega t)]\,\hat{\jmath} \qquad (23)$$

where u'_s and v'_s are the amplitudes of oscillation at the source about $\overline{U}$ and $\overline{V}$. The velocity

9
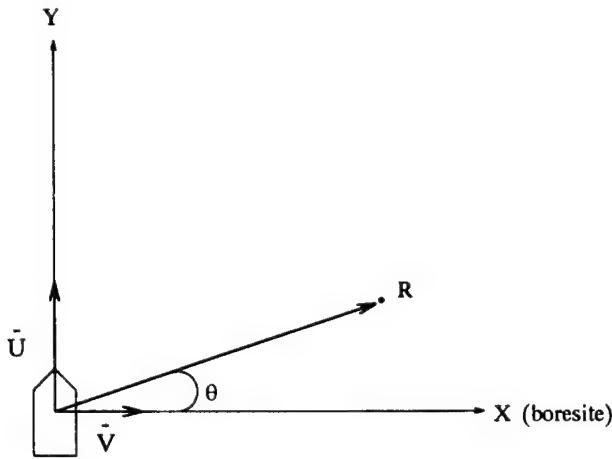
Figure 3. Receive array co-ordinate system.

at the receiver is

$$\vec{V}_R = [\overline{V} + v_R'\cos(\omega t)]\,\hat{\imath} + [\overline{U} + u_R'\cos(\omega t)]\,\hat{\jmath} \tag{24}$$

The projections of these velocities along θ are

$$\vec{V}_S \cdot \hat{\imath} = [\overline{U}\sin\theta + \overline{V}\cos\theta] + [u_S'\sin\theta + v_S'\cos\theta]\cos(\omega t) \tag{25}$$

$$\vec{V}_R \cdot \hat{\imath} = [\overline{U}\sin\theta + \overline{V}\cos\theta] + [u_R'\sin\theta + v_R'\cos\theta]\cos(\omega t) \tag{26}$$

Comparing equations (25) and (26) with equations (16) and (18), V_{SH}, V_S and V_R are found as

$$V_{SH} = \overline{U}\sin\theta + \overline{V}\cos\theta \tag{27}$$

$$V_S = u_S'\sin\theta + v_S'\cos\theta \tag{28}$$

$$V_R = u_R'\sin\theta + v_R'\cos\theta \tag{29}$$

The phase then becomes, from equation (20),

$$\psi = 2\pi\left[\frac{[V_T + \overline{U}\sin\theta + \overline{V}\cos\theta]\,t}{\lambda} + \frac{VT}{2\pi\lambda}\sin(\frac{2\pi t}{T})\right] \tag{30}$$

In writing equation (30), the velocities of the transmit and receive antennas have been taken as equal, such that $u_S' = u_R' = U'$ and $v_S' = v_R' = V'$. These conditions provide the worst case results in determining the ship-induced Doppler. The unsteady velocity V is defined by

$$V = U'\sin\theta + V'\cos\theta \tag{31}$$

10

Periodic Ship Motions

Equation (30) determines the modification of the phase due to periodic ship motions. The Doppler spectrum of the modulation signal, defined by equation (21), with the phase given by equation (30) has been discussed by Oppenheim et al. (1983). For $VT/\lambda \ll 1$, the spectrum consists of the expected Doppler peak corresponding to $V = 0$ and two sideband peaks symmetrically placed around the expected peak at a frequency spacing of $\pm 2\pi/T$. As VT increases, the two sideband peaks also increase in magnitude and additional sideband peaks appear. Examples of this phenomenon are shown in Figure 4. This figure shows the behavior of the spectrum for increasing V for a fixed period T of 20 s. To facilitate the comparisons to OSCR data, the power spectrum is based on 512 samples of equation (21), with a sampling interval of 0.32768 s. Without loss of generality, the amplitudes have been taken as $A = 1$ and $B = 0$ in equation (21), the mean ship velocities have been taken as $\overline{U} = \overline{V} = 0$ in equation (30), and V_T has been set to the Bragg wave phase speed given in equation (1). Each figure indicates the dB difference between the expected Doppler peak and the secondary peak. The variations of dB difference with changes in periodicity, T, and velocity, V, are shown in Figure 5. FFT truncation errors (Brigham, 1974) lead to the curves not falling exactly on top of each other. Generally, peaks more than 6 dB down from the primary peak are ignored by the peak picking routine. Hence, from Figure 5, VT values of less than 2.8 m are necessary to avoid processing contamination due to periodic ship motions.

Mean Ship Motions

As indicated by equation (30), the measured radials will need to be corrected for the forward and drift motions of the ship. This correction can be done by shifting the spectra, or by correcting the resultant radials. From equations (9) and (30), the corrected radials, R_C, will therefore be

$$R_C = FF * DTV - (\overline{U}\sin\theta + \overline{V}\cos\theta) \tag{32}$$

The frequency correction is of the same form,

$$f_{SHIFT} = -(\frac{\overline{U}\sin\theta + \overline{V}\cos\theta}{\lambda}) \tag{33}$$

and would be applied to the raw spectra before subsequent analysis. To minimize the corrections

11
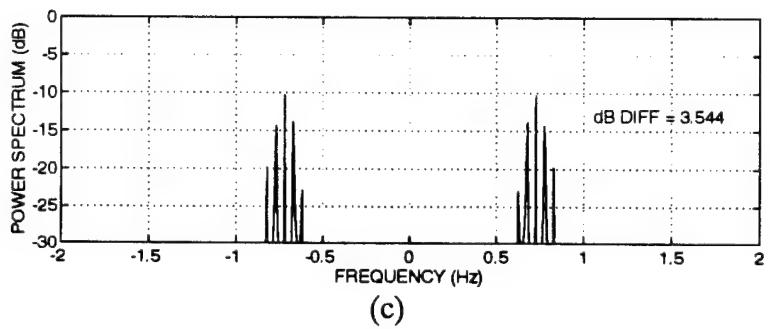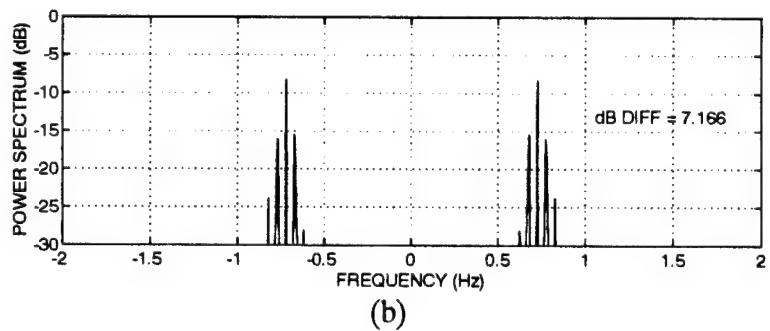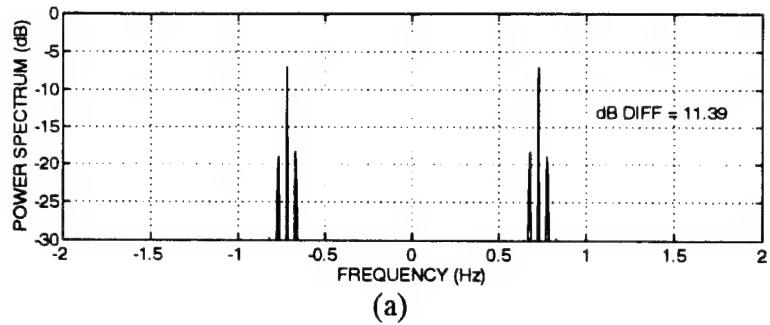
Figure 4. Power spectrum of the modulation signal for a period $T = 20$ s. (a) $V = 0.10$ m/s; (b) $V = 0.15$ m/s; (c) $V = 0.2$ m/s.
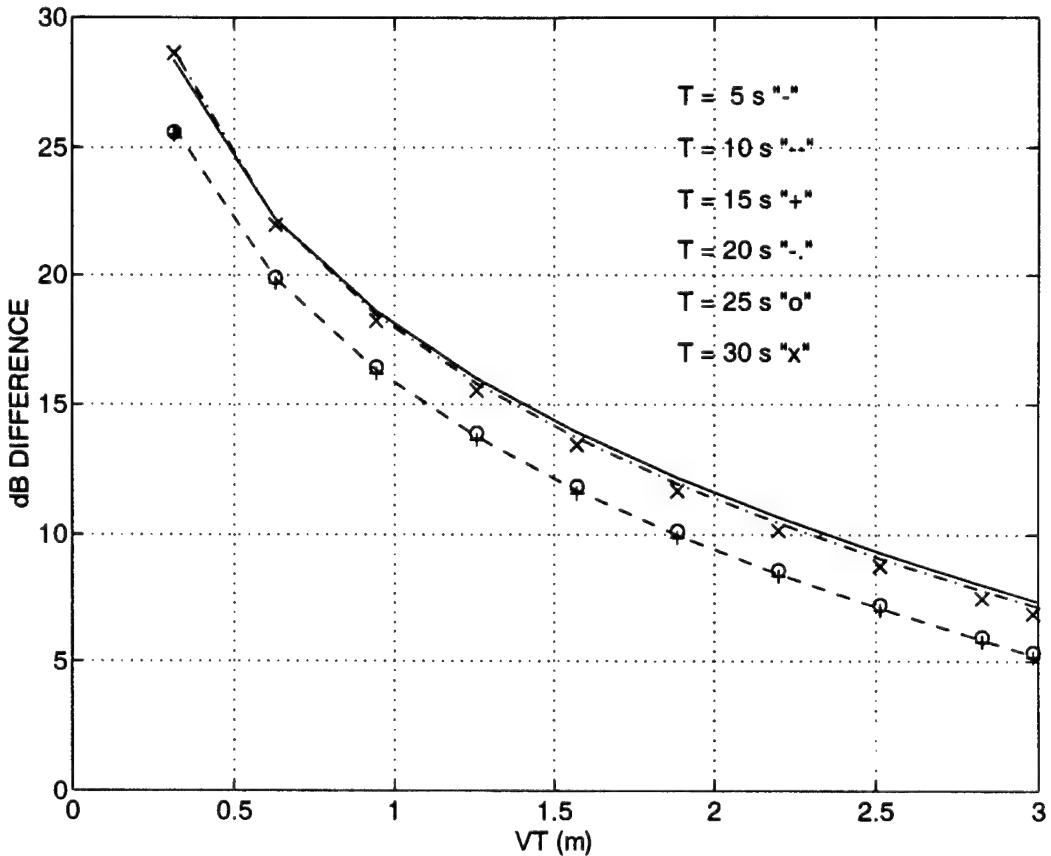
Figure 5. dB difference between spectral value at expected spectral peak and spectral value at maximum sideband peak as a function of the oscillatory displacement *VT*.

to the radial currents due to mean ship motions, the ship was operated at the lowest speed for which directional control could still be maintained. Typically this speed was on the order of $\overline{U}$ = 1.0 m/s and the heading was maintained to within ±2° of the mean heading. The value of the drift velocity $\overline{V}$ was dependent on the direction of the current relative to the ship and ranged from 0 to about 1.5 m/s. Details of these results will be discussed later.

The movement of the ship also affects the grid cell structure. The grid, as defined by the OSCR system, is a series of range and bearing variables unique to each cell evaluated from the site position. Thus, as the ship moves during the transmit and receive cycle, the cells change position in the Earth coordinate system but maintain their orientation relative to the ship. The net result of this movement is a larger area of return attributed to the cell position than would otherwise be the case. The reference grid is taken as that one associated with the mean location

of the ship during the transmit-receive cycle. Then the sampled cell width (the tangential arc subtended by the 3 dB down point of the receive array) becomes the nominal cell width plus the distance $\overline{U} T_T / 2$ on each side of the nominal cell width, where T_T is the time duration of the cycle. Similarly, the sampled cell depth becomes the nominal cell depth given by equation (5) plus the distance $\overline{V} T_T / 2$ on each side of the nominal cell depth. For $T_T = 300$ s, corresponding to the OSCR cycle, and $\overline{U} \approx 1.0$ m/s, the half-increase in the nominal cell width is 150 m. The half-increase in the nominal cell depth ranges from 0 to about 225 m.

Ship Motion Measurements

The shipboard log recorded position and heading data every two minutes. The position of the vessel was obtained from Global Positioning System (GPS) readings giving latitude and longitude, and the heading was recorded as a bearing from true north. The GPS readings during the transmit-receive cycle were used to determine the mean ship velocities $\overline{U}$ and $\overline{V}$.

In addition, a six channel piezoresistive accelerometer system was installed on the COLUMBUS ISELIN at the locations indicated in Figure 6 (Skop et al., 1994). Three of the accelerometers were mounted on a triaxial block aligned parallel to the ship fixed x, y and z axes. Two accelerometers were mounted on a biaxial block aligned to the ship fixed x and z axes. The biaxial block was located 5.27 m directly inboard of the triaxial block. The final accelerometer was mounted on a uniaxial block aligned to the ship fixed z axis and located 3.20 m directly aft of the triaxial block.

The local linear velocity vector $\vec{U}_i$ at any point i on the ship is given by

$$\vec{U}_i = u_i \hat{\imath} + v_i \hat{\jmath} + w_i \hat{k} \tag{34}$$

where $\hat{\imath}$, $\hat{\jmath}$ and $\hat{k}$ are the unit vectors and u_i, v_i and w_i are the local velocity components along the ship fixed x, y and z axes respectively. The ship angular velocity vector $\vec{\Omega}$ is given by

$$\vec{\Omega} = p\hat{\imath} + q\hat{\jmath} + r\hat{k} \tag{35}$$

where p is the roll rate about the x axis, q is the pitch rate about the y axis, and r is the yaw rate about the z axis. The accelerometer data are used to determine $\vec{\Omega}$ and $\vec{U}_i$. Letting the subscripts t, b and u denote the triaxial, biaxial and uniaxial accelerometer blocks, respectively,

14
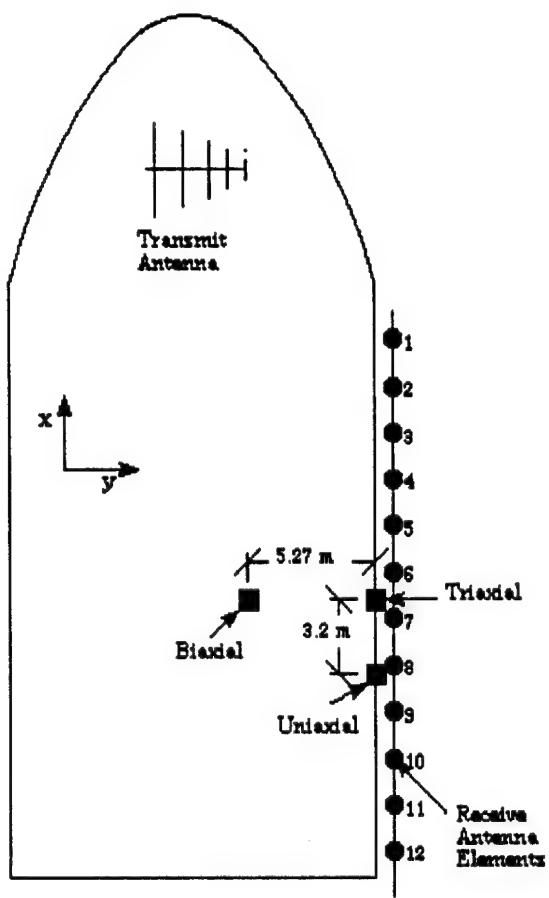
Figure 6. The OSCR and accelerometer system arrangements aboard the COLUMBUS ISELIN. Not to scale.

the values of $\vec{\Omega}$ (or p, q and r) and $\vec{U}_i$ are

$$p = \frac{w_t - w_b}{5.27}, \quad q = \frac{w_u - w_t}{3.20}, \quad r = \frac{u_b - u_t}{5.27} \tag{36}$$

and

$$\vec{U}_i = \vec{U}_t + \vec{\Omega} \times \vec{R}_{ti} \tag{37}$$

where $\vec{R}_{ti}$ is the position vector from the triaxial block to the point i. Equation (37) was used to determine the oscillatory velocity V defined by equation (31).

15

SUMMARY OF MOORED SHIP EXPERIMENT

The moored ship OSCR experiment conducted in December 1993 is discussed in detail in Skop et al. (1994). The relevant features of this experiment are summarized here.

Grid for the Stationary Site

The RV COLUMBUS ISELIN, for the stationary phase, was four-point anchored a distance of about 5 km off the south end of Key Biscayne. The relative positions of the ship and shore sites, and the grid coverage of domain in which radial currents were measured, are shown in Figure 7. One set of cells lies along the line-of-sight between the ship and shore-based sites. The other set of cells is in the region where vector currents were constructed from the measured radials.

Oscillatory Ship Motions

Because of the four-point, fore-aft anchoring scheme, and calm weather conditions, the oscillatory ship motions during the stationary phase of the experiment were constrained. The variations in heading about the nominal moored heading were within ±2°.

For the OSCR configuration aboard the COLUMBUS ISELIN, the transmit antenna, for which $\vec{R}_{t1}$ in equation (37) was given by {32.5 m, -5.5 m, -5.5 m}, experienced the maximum motions of any of the antenna elements. Hence, the "worst-case" effects of oscillatory ship motions are determined by setting U' and V' in equation (31) to their transmit antenna values. For the moored configuration, $U' < 0.2$ m/s and can be ignored in the evaluation of VT. A typical V' record at the transmit antenna, obtained from the accelerometer measurements, is shown in Figure 8a, and the corresponding VT versus frequency plot is shown in Figure 8b. The peak value of VT is on the order of 1.0 m. Transposing this value of VT to Figure 5, the sideband peaks due to periodic ship motions during the stationary phase of the experiments were at least 15 dB down from the true Doppler peaks.

16
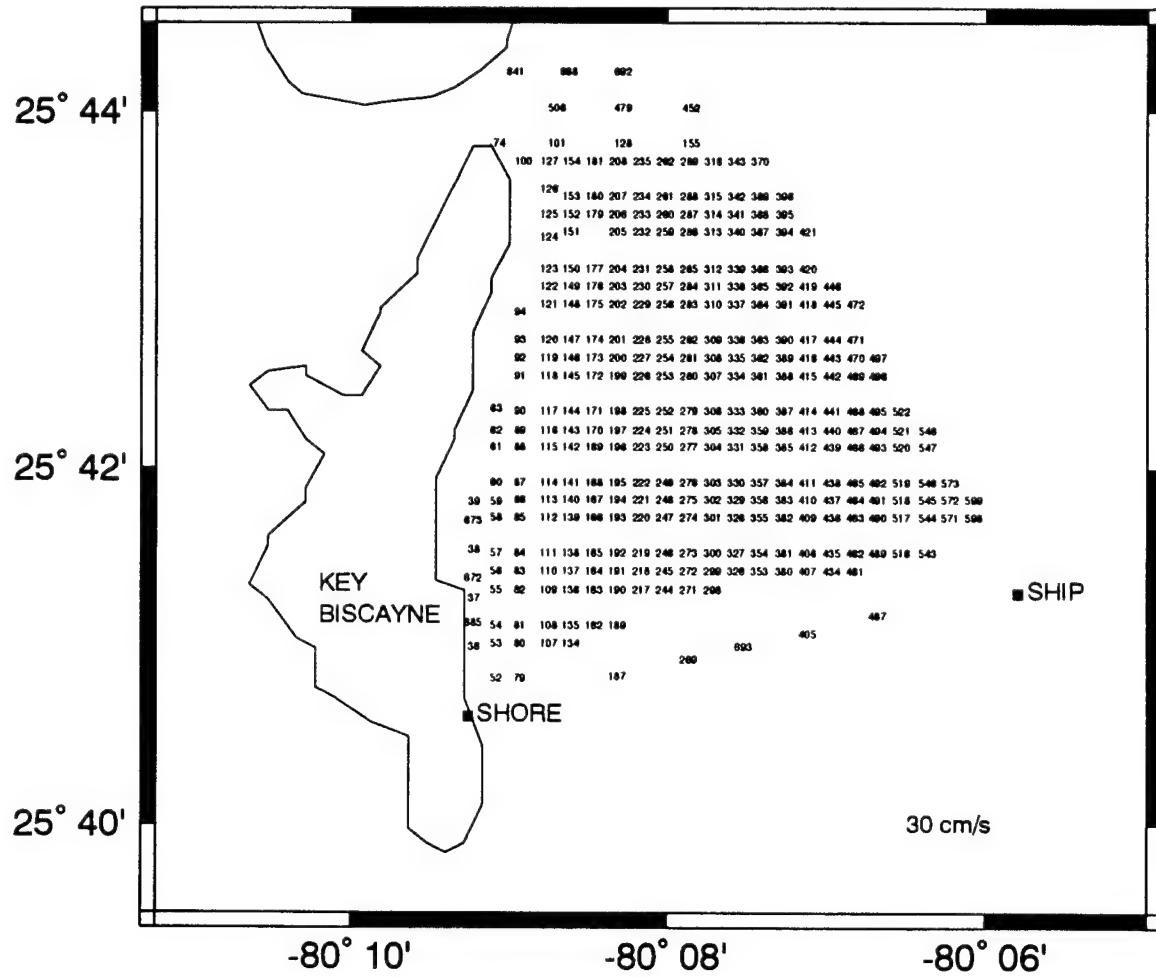
Figure 7. OSCR configuration for the shipboard experiment.
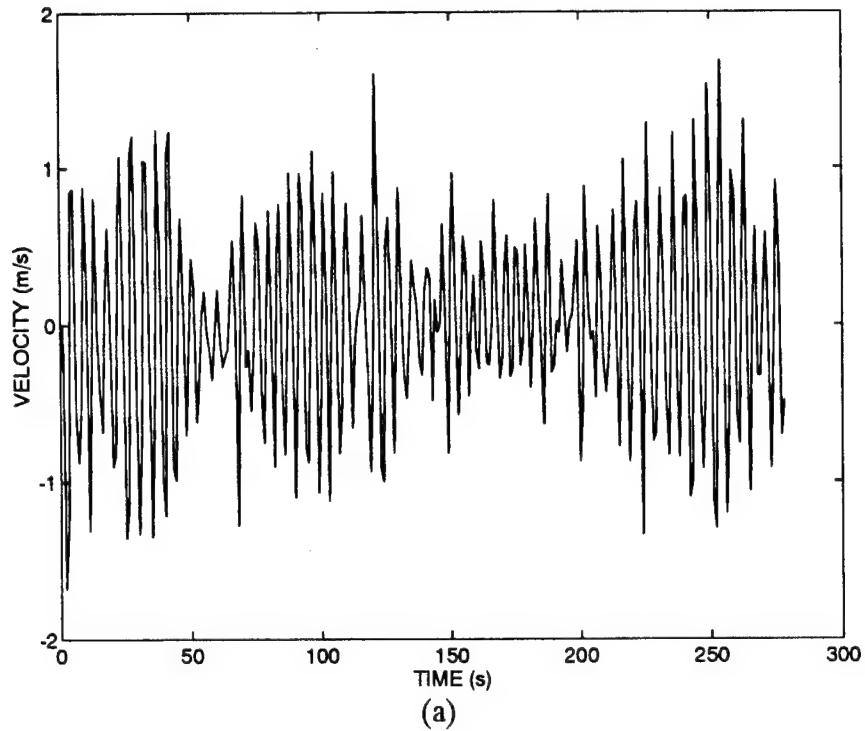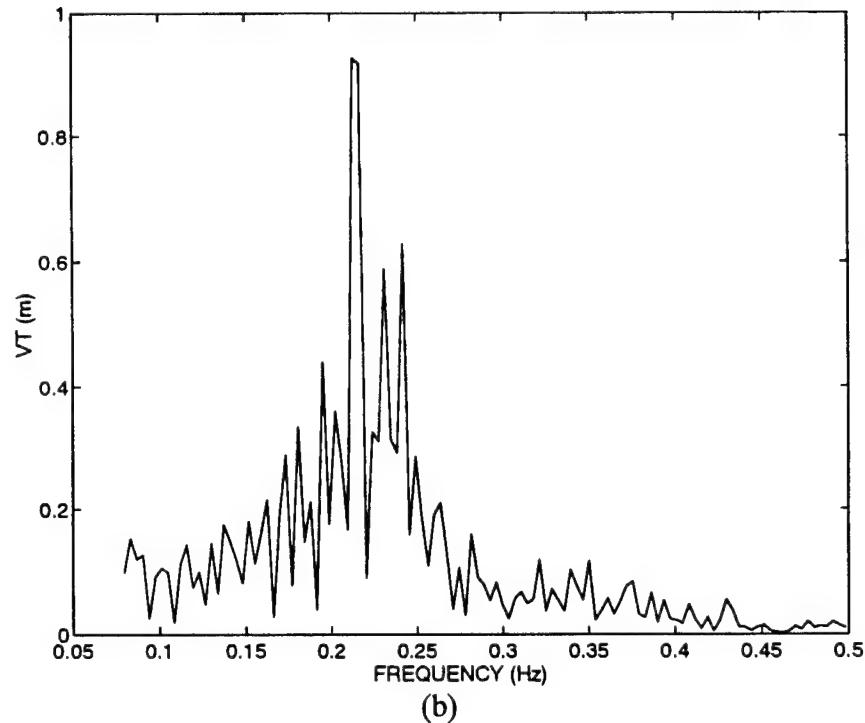
Figure 8. Transmit antenna motions for the OSCR moored ship experiment during December 1993. (a) y-direction velocity V'; (b) VT.
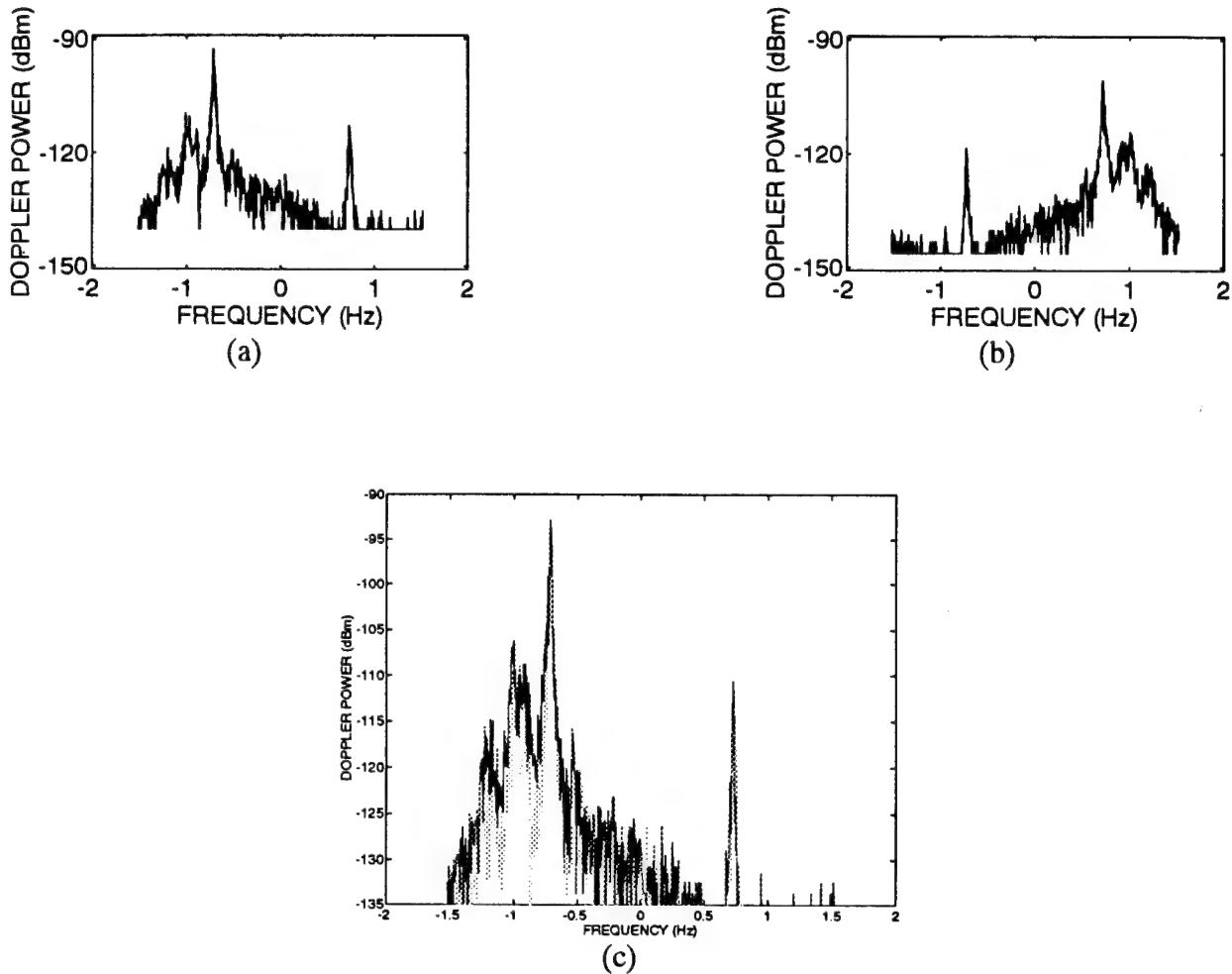
Figure 9. Doppler spectra from cell 693. (a) Ship site; (b) shore site; (c) overlaid spectra.

Comparison of Co-Linear Spectra

Cell number 693 lies on the co-linear line-of-sight between the ship and shore-based radar positions, as shown in Figure 7. Hence, in the absence of ship motion and superstructure effects, the ship and shore-based Doppler spectra from cell 693 should be mirror images. The spectra received from cell 693 at the ship and shore-based sites are shown for a particular sample time in Figures 9a and 9b, respectively. The shore spectrum reversed about the zero frequency and overlaid on the ship spectrum is shown in Figure 9c. The Doppler power scales have been matched, as this scale gives relative power and is therefore arbitrary. The goodness of the match between the two spectra is evident, even down to tertiary peaks. This agreement demonstrates that, for the OSCR configuration aboard the COLUMBUS ISELIN, the shipborne ground wave

surface current radar was unaffected by the vessel's superstructure or periodic motions and functioned in the same manner as the shore-based system.

MOVING SHIP EXPERIMENT - KEY BISCAYNE

Conduct of the Experiment

In December 1993 and July 1994, the COLUMBUS ISELIN conducted north to south passes off the east coast of Key Biscayne to examine the possibility of generating surface current maps from a moving platform. The configurations of the OSCR sites aboard the ship and on Key Biscayne were the same as those for the moored ship experiment. The weather during the dates of the experiments was characterized by winds of less than 7 m/s and light seas. The vessel maintained a speed of approximately 1 m/s during the transmit-receive cycles. The first transmit-receive cycle coincided with the ship located towards the northern end of the shore-based grid. In the July experiment, the ship then transited south and the next transmit-receive cycle coincided with the ship located towards the southern end of the shore-based grid. The ship trajectory from immediately preceding to immediately following each data collection cycle is shown in Figure 10. Due to the asymmetrical grid configuration relative to the ship, the overlapping coverage of the northern leg and the shore-based site is much reduced compared to the overlapping coverage of the southern leg and the shore-based site, as indicated in Figure 11. As mentioned previously, the grid position attributed to the ship is taken as that one associated with the mean location of the ship during the transmit-receive cycle.

Mean Ship Motions

The values of the mean ship velocities $\overline{U}$ and $\overline{V}$ were obtained from two or three successive GPS readings during each transmit-receive cycle. The value of the mean ship heading was obtained from two or three successive ship compass readings during each cycle. The heading deviation, or yaw, was obtained by time integration of the yaw rate r, defined by equation (36), continuously during each cycle. The mean ship velocities, headings and heading variations for the north to south passes off Key Biscayne are summarized in Table 1. The mean
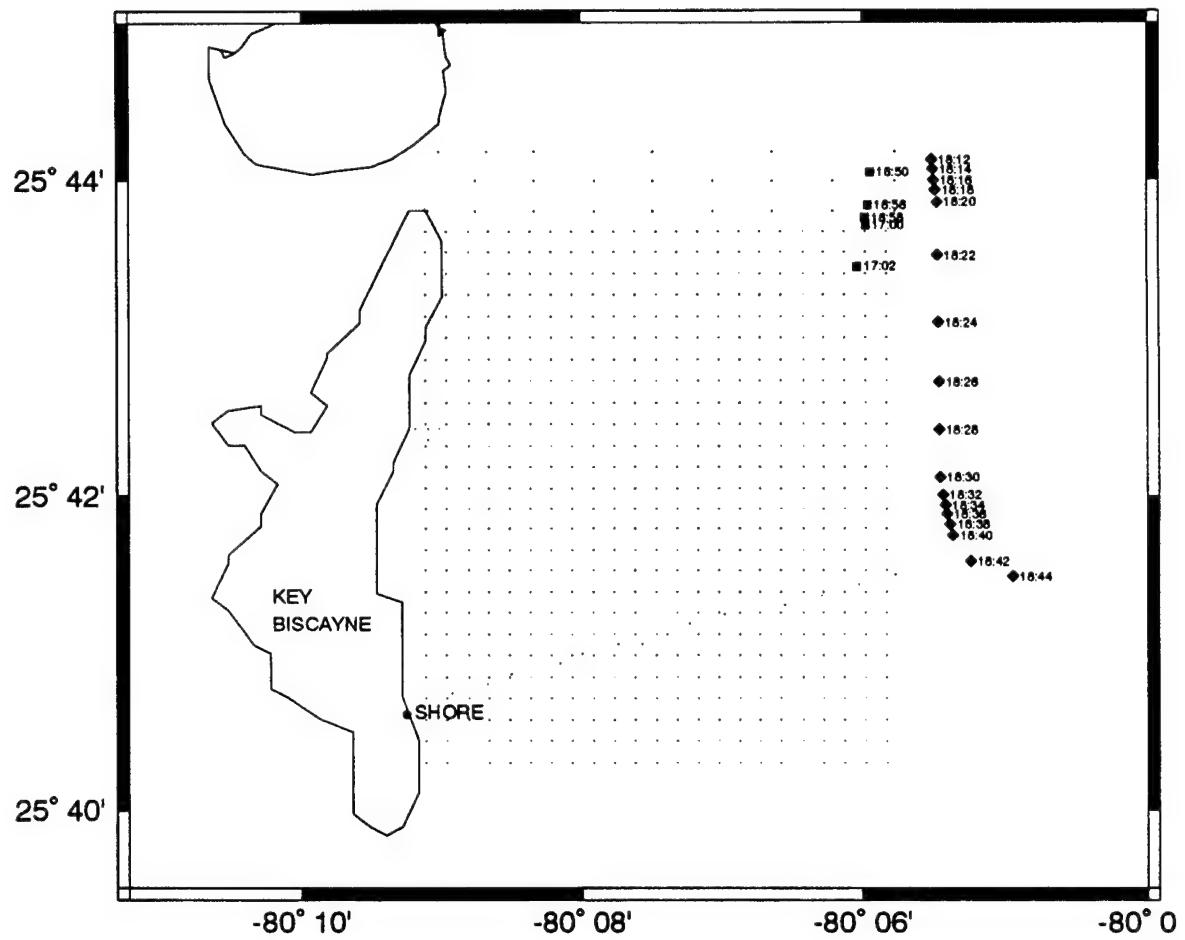
Figure 10. Ship trajectories for the Key Biscayne moving ship experiment. December 1993 (■);
July 1994 (♦).

Table 1. Mean velocities, headings, and heading variations for the Key Biscayne legs.

Key Biscayne	$\overline{U}$ (m/s)	$\overline{V}$ (m/s)	Heading (deg)	Yaw (deg)
Dec 93 N	0.75	0.05	176.1	±0.6
Jul 94 N	1.13	-0.03	175.0	±0.6
Jul 94 S	1.08	-0.25	173.9	±0.9

Table 2. Periodic ship motions for the Key Biscayne legs.

Key Biscayne	U' (m/s)	V' (m/s)	$(U'T)_{max}$ (m)	$(V'T)_{max}$ (m)
Dec 93 N	±0.4	±1.1	0.10	0.35
Jul 94 N	±0.3	±0.4	0.23	0.15
Jul 94 S	±0.3	±0.5	0.27	0.25

ahead velocities $\overline{U}$ were all on the order of 1 m/s and the mean drift velocities $\overline{V}$ were substantially smaller. The heading variations for all three legs were bounded by ±1° based on the yaw records.

Oscillatory Ship Motions

The periodic ship motions recorded during the three Key Biscayne legs are summarized in Table 2. Both U' and V' were measured at the transmit antenna which experienced the maximum motions of any of the antenna elements. Accordingly, the values of $(U'T)_{max}$ and $(V'T)_{max}$ represent the maximum effects of oscillatory ship motions on the ship-induced Doppler spectrum modulations as defined by equations (30) and (31). In equation (31), setting the trigonometric terms to unity gives the maximum summed periodic velocity and $(VT)_{max} = (U'T)_{max} + (V'T)_{max}$ gives the maximum summed modulation value. The largest value of $(VT)_{max}$ for the Key Biscayne passes was 0.52 m for the July 1994 southern leg. Transposing

23

this value to Figure 5, the motion-induced sideband peaks during the Key Biscayne legs were at least 20 dB down from the expected Doppler peaks.

Spectral Returns

Doppler spectra received from cells along the boresite of the receive array are shown in Figures 12, 13 and 14 as a function of increasing distance from the ship for the December 1993 northern leg, the July 1994 northern leg and the July 1994 southern leg, respectively. In most cases, the spectra for the cells between approximately 1.0 and 5.0 km distance, which corresponds to the mid-range of the OSCR domain, contain discernable peak spectral pairs at the expected 2 *FBG* separation. This separation and the selected peak spectral pairs are indicated in Figures 12, 13 and 14. The peaks are somewhat broadened compared to those typically observed from a shore-based site (see Figure 7) and are also reduced in power relative to the secondary peaks. This reduction in peak power is directly attributable to the peak broadening which, in turn, is due to broad-band ship oscillatory motions. At around the 5.0 km distance, the spectral structure decays to the extent that no reasonable peak pair can be identified.

Doppler spectra received from mid-range cells are shown in Figures 15, 16 and 17 as a function of the cell angle θ, ranging from +45° to -45° from the boresite, for the December 1993 northern leg, the July 1994 northern leg and the July 1994 southern leg, respectively. Peak pair selection is possible out to the extreme ±45° angles of the system, although at smaller angles there is a noticeable increase in the quality of the spectra.

As demonstrated in the moored ship experiment, analysis of the spectral returns from a common cell lying on the line-of-sight between the ship and shore-based sites indicates the type of degradation experienced by the ship-based spectrum due to ship motions. For the moving ship experiment, the grid is carried along with the ship and exactly common ship and shore-based cells along the line-of-sight are the exception. However, ship and shore-based cells in close proximity to each other and to the line-of-sight are compared in Figures 18a, 18b and 18c for the December 1993 northern leg, the July 1994 northern leg and the July 1994 southern leg, respectively. The cells compared are within 125 m of each other and within 75 m of the line-of-sight. The ship-based spectra are shifted in frequency, as given by equation (33), to correct for mean ship motions and then reversed about the zero frequency and overlaid on the coinciding
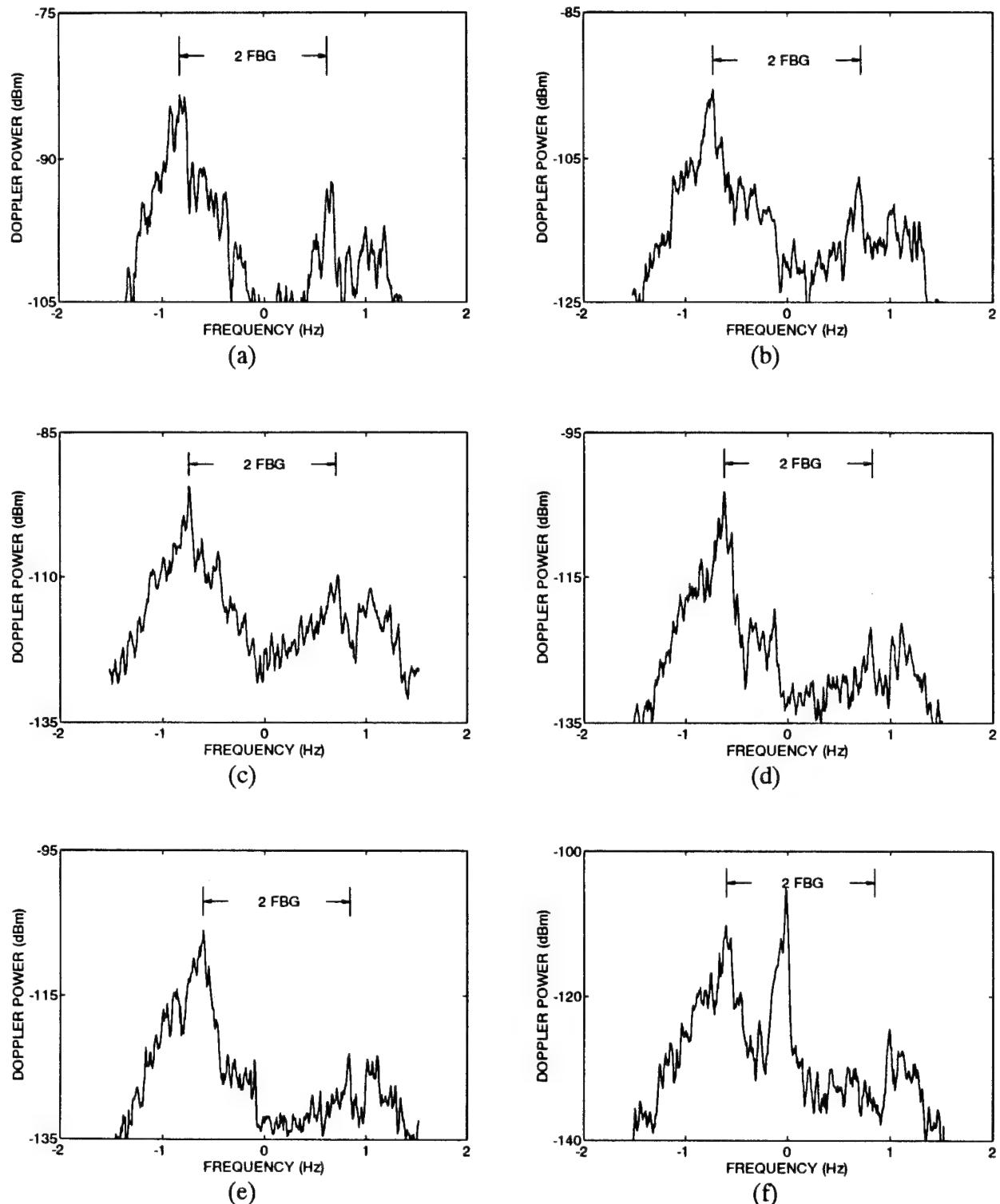
Figure 12. Doppler spectra from cells along boresite versus increasing distance from ship during the December 1993 northern leg. (a) 839 m; (b) 2198 m; (c) 2475 m; (d) 4136 m; (e) 4414 m; (f) 4969 m.

25
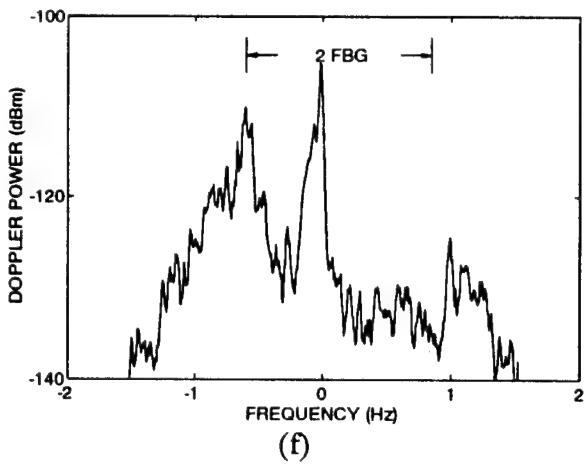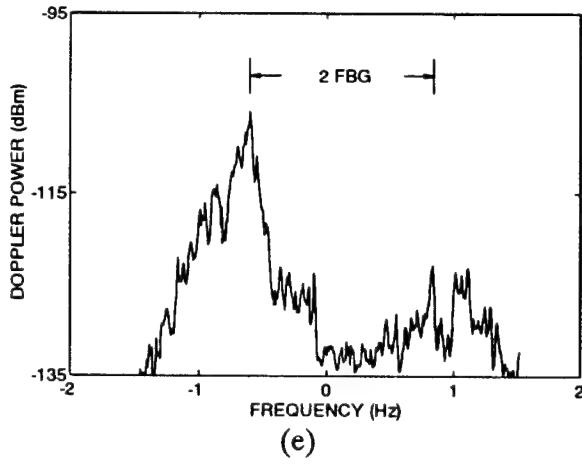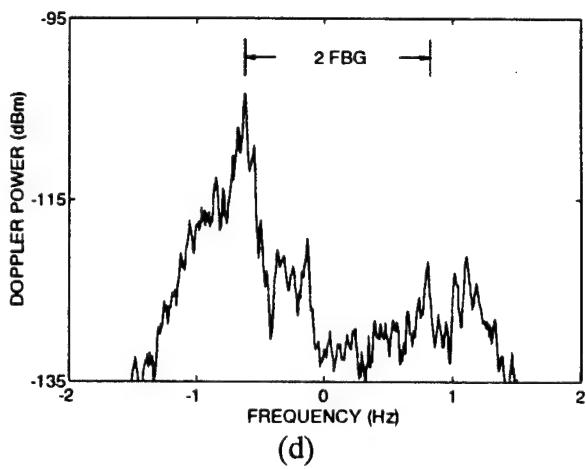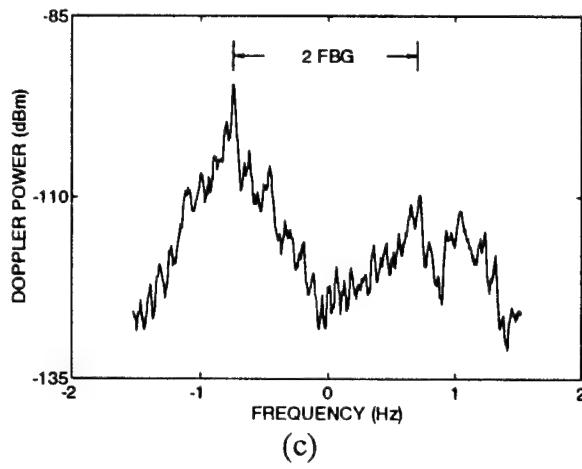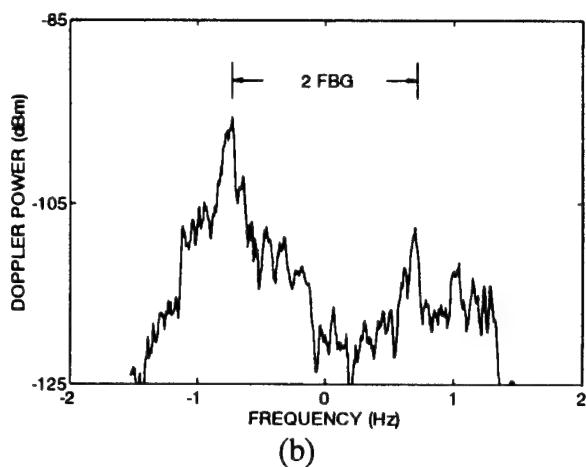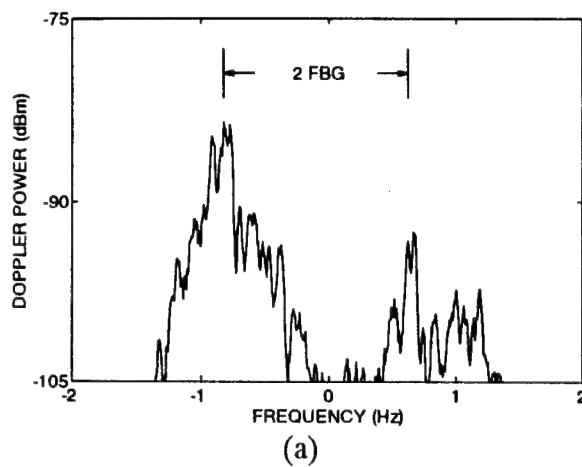
Figure 13. Doppler spectra from cells along boresite versus increasing distance from ship during the December 1993 northern leg. (a) 839 m; (b) 2198 m; (c) 2475 m; (d) 4136 m; (e) 4414 m; (f) 4969 m.
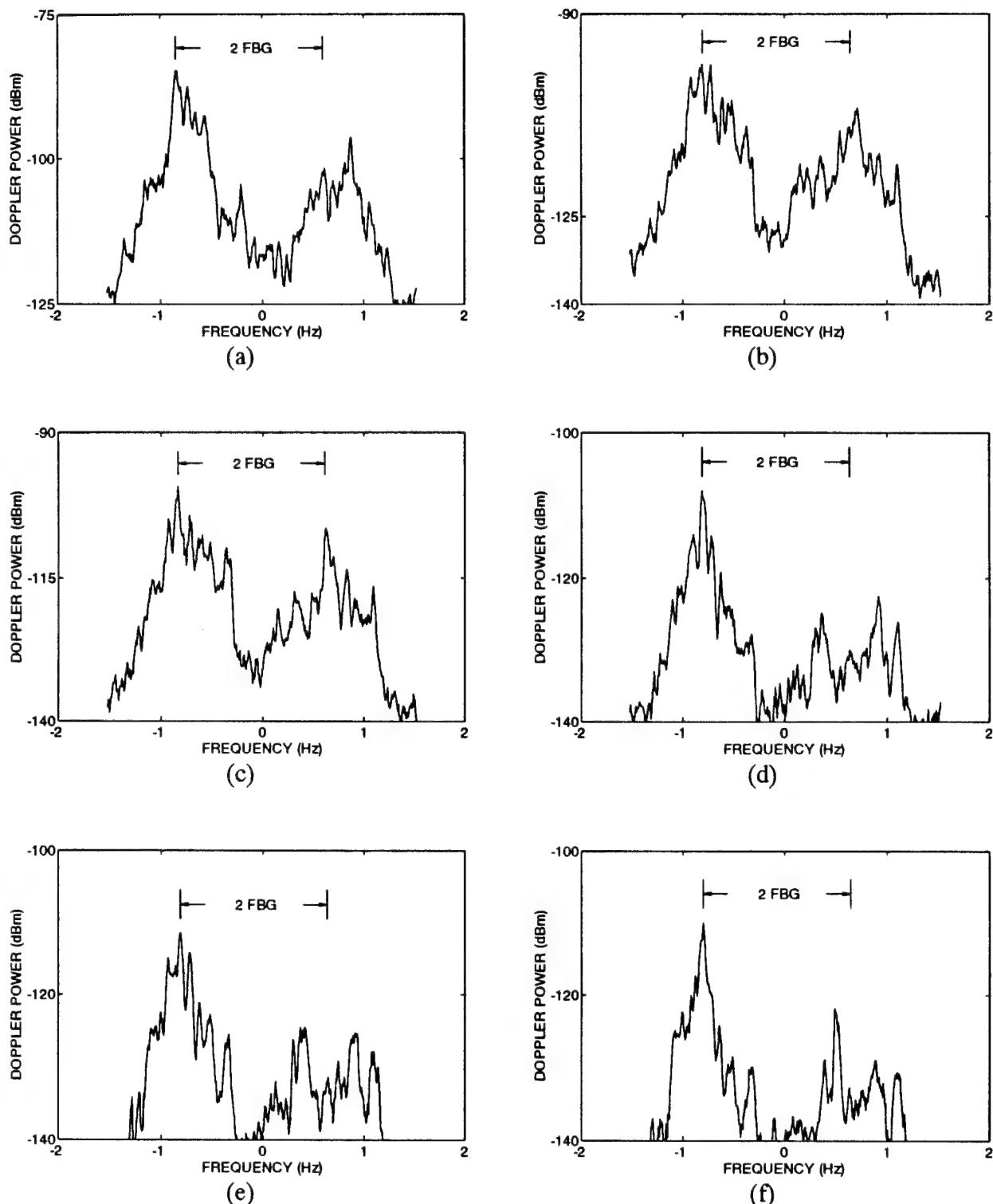
Figure 14. Doppler spectra from cells along boresite versus increasing distance from ship during the July 1994 southern leg. (a) 839 m; (b) 2198 m; (c) 2475 m; (d) 4136 m; (e) 4414 m; (f) 4969 m.

27
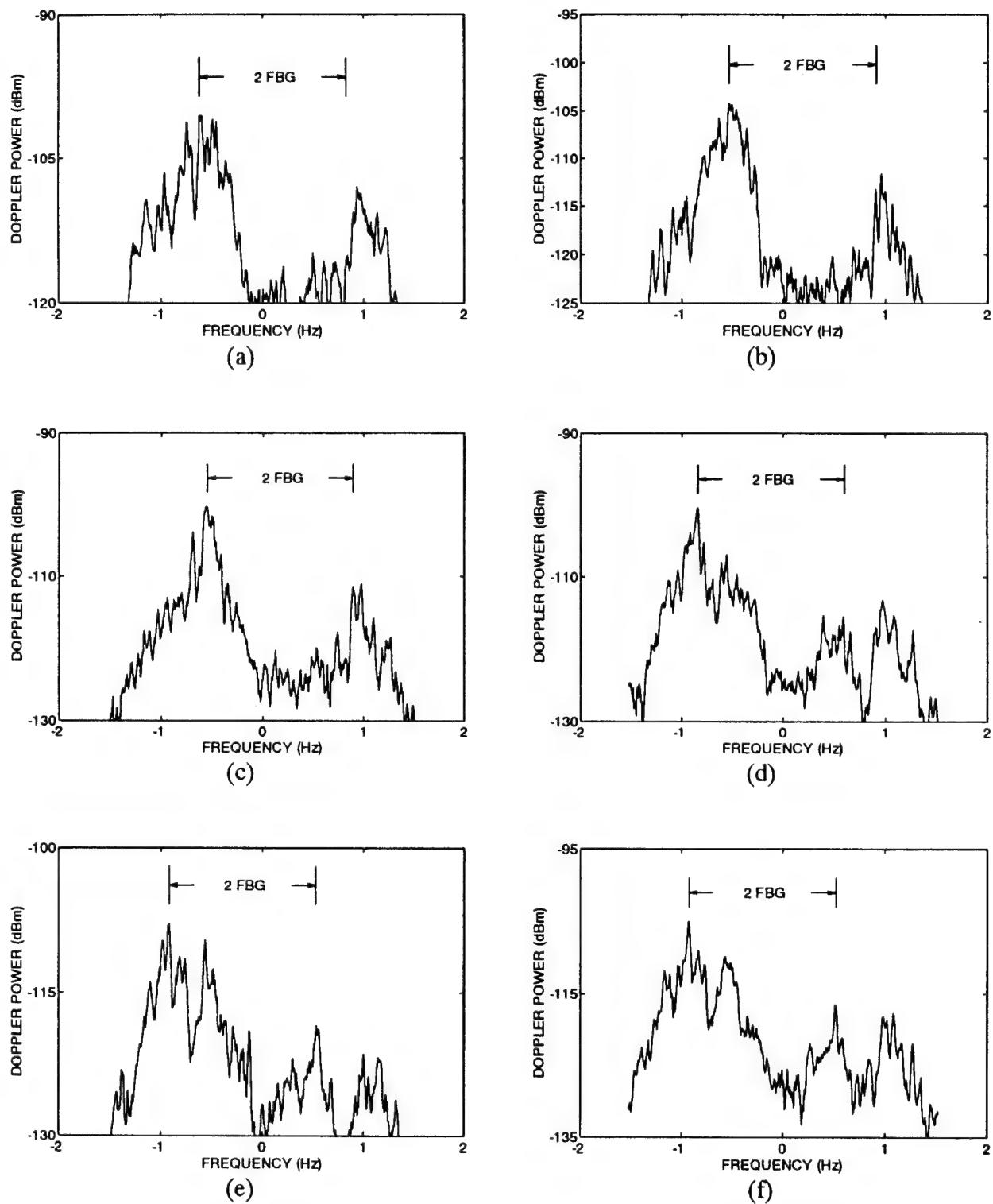
Figure 15. Doppler spectra from mid-range cells, 3.5 to 4.0 km, versus cell angle from the boresite for the December 1993 northern leg. (a) 45°; (b) 35°; (c) 25°; (d) -25°; (e) -35°; (f) -45°.

28
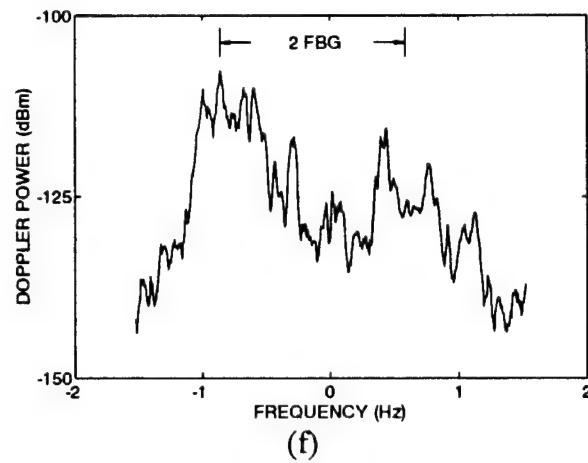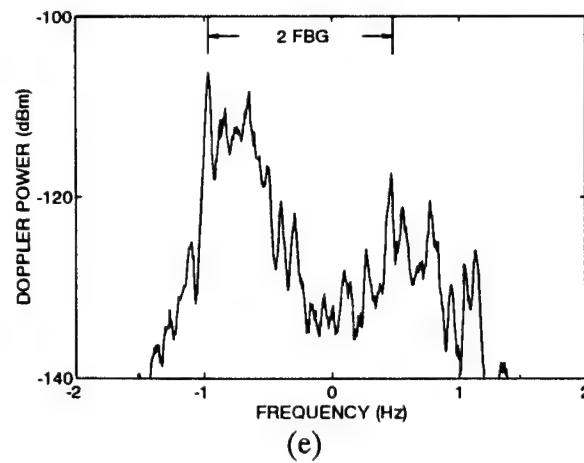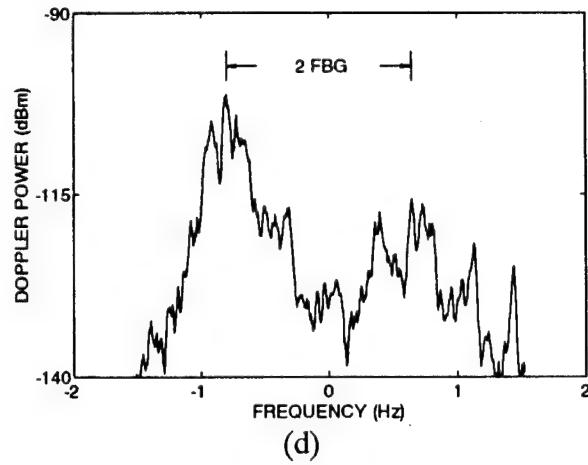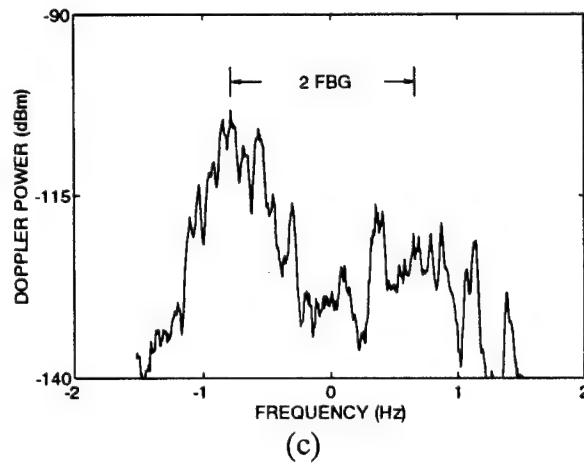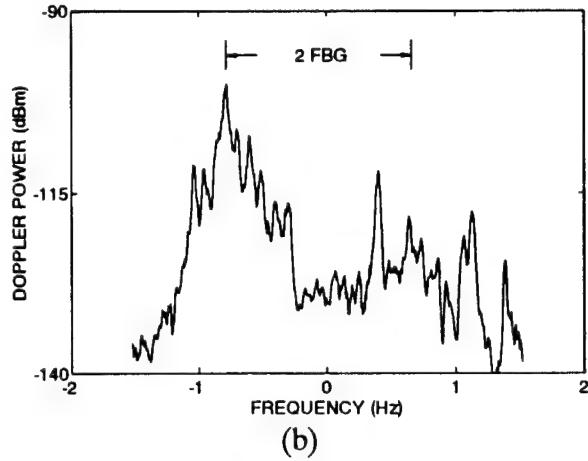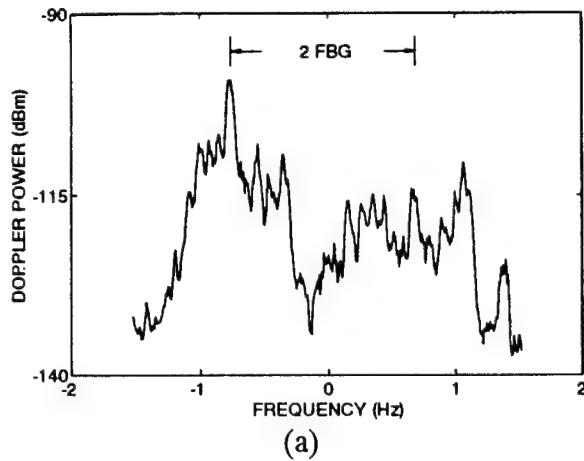
Figure 16.   Doppler spectra from mid-range cells, 3.5 to 4.0 km, versus cell angle from the boresite for the July 1994 northern leg. (a) 45°; (b) 35°; (c) 25°; (d) -25°; (e) -35°; (f) -45°.
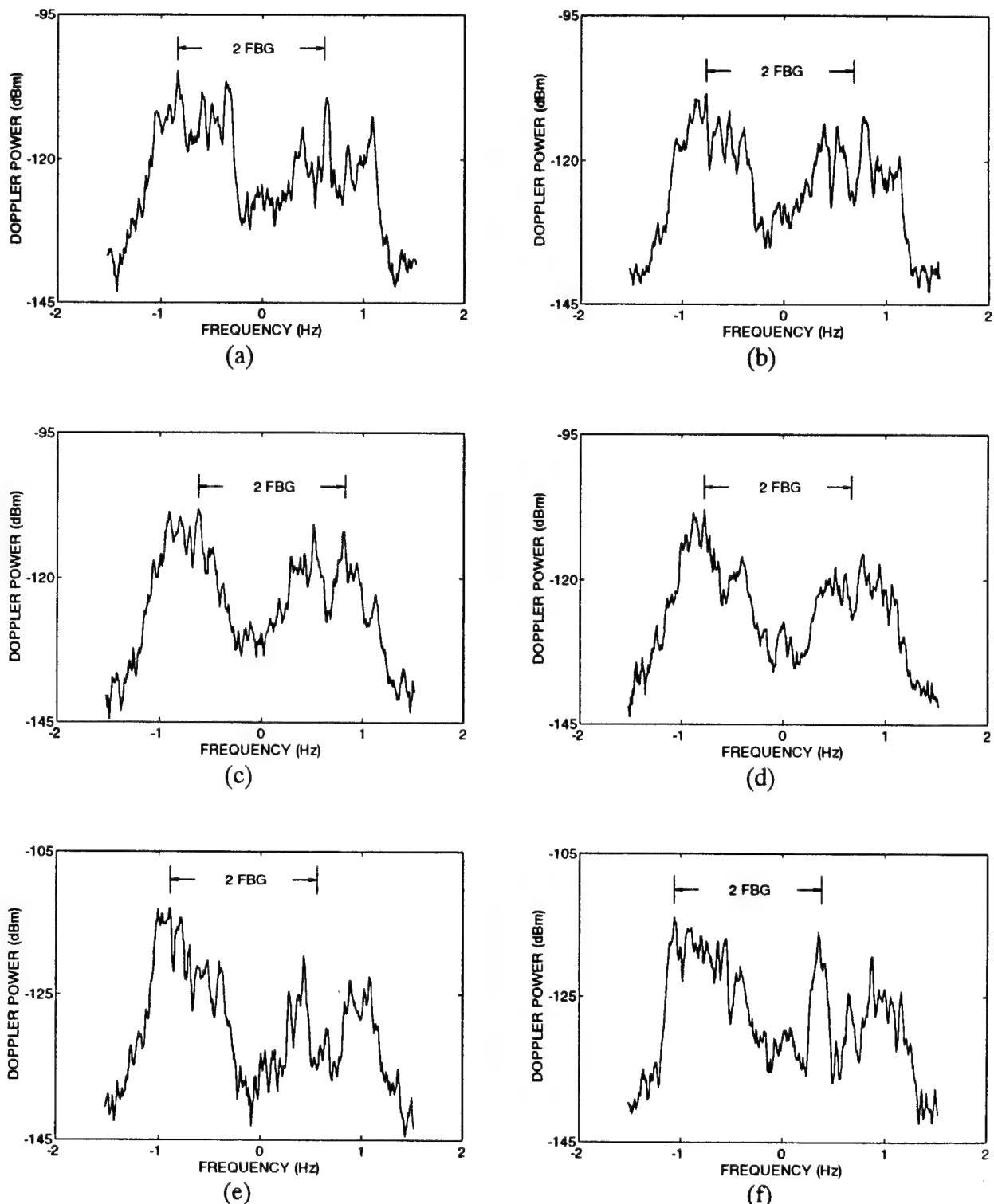
Figure 17. Doppler spectra from mid-range cells, 3.5 to 4.0 km, versus cell angle from the boresite for the July 1994 southern leg. (a) 45°; (b) 35°; (c) 25°; (d) -25°; (e) -35°; (f) -45°.

30
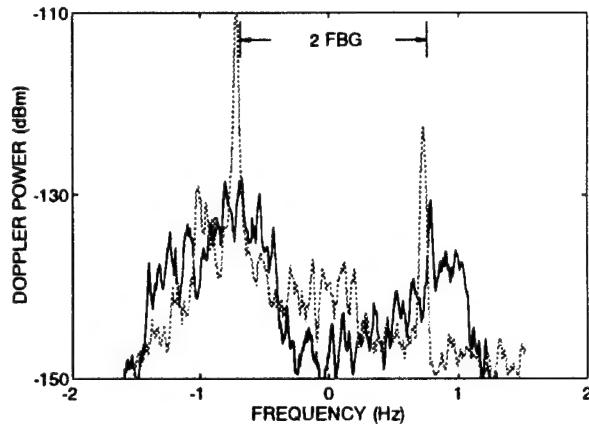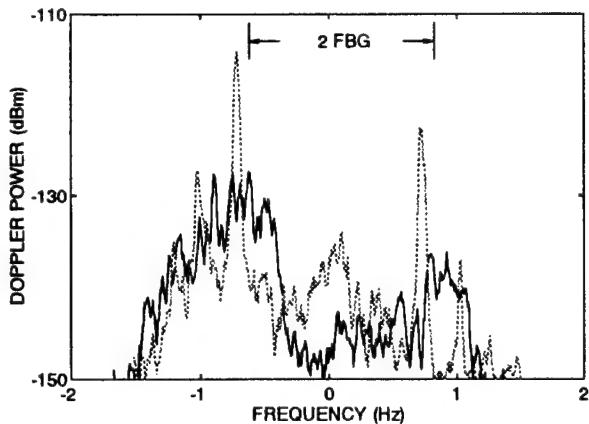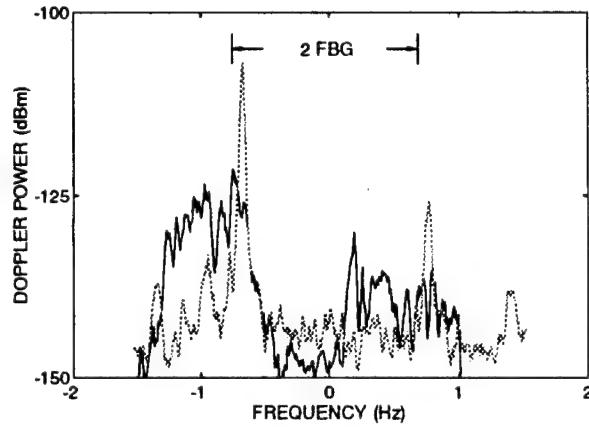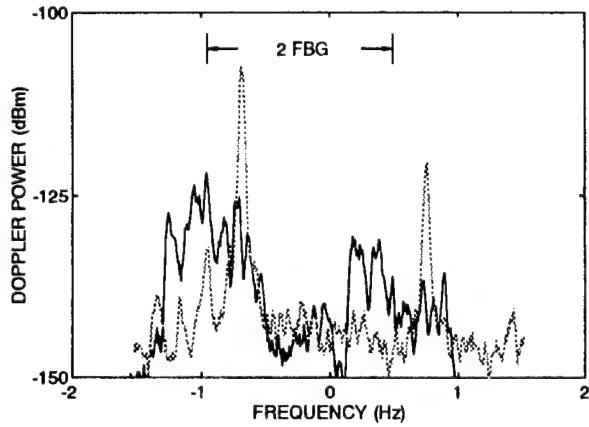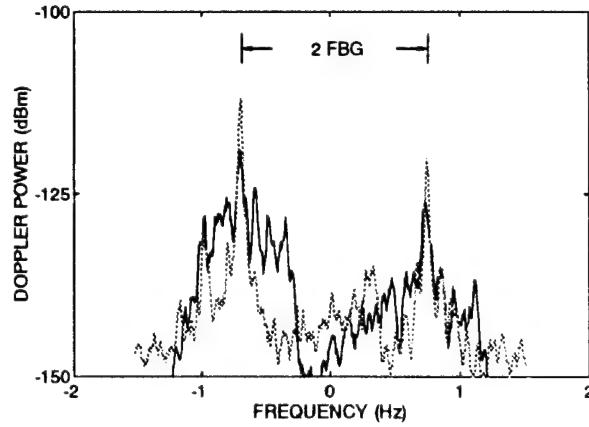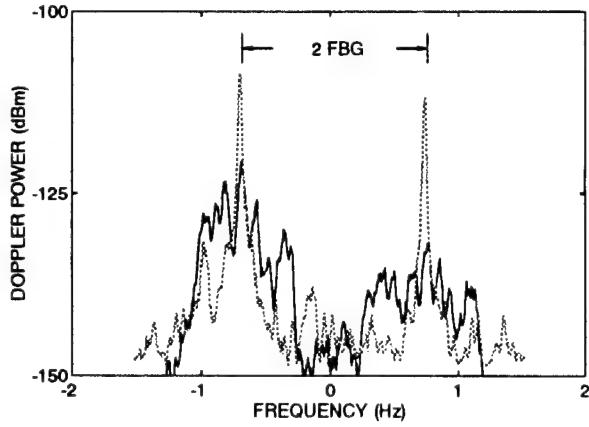
Figure 18. Comparisons of frequency corrected ship-based spectra (solid lines) and line-of-sight shore-based spectra (dashed lines). The **2 FBG** separations indicated correspond to the ship spectra. (a) December 1993 northern leg; (b) July 1994 northern leg; (c) July 1994 southern leg.

31

shore-based spectra. The $2\,FBG$ separation shown in the figures indicates the selected peak spectral pairs of the ship spectra.

For the December 1993 northern leg (Figure 18a), the peak spectral pairs of the mirror imaged ship spectra are displaced slightly to the positive frequency side of the peak spectral pairs of the shore spectra. The peak pair displacement is most likely due to GPS errors in the ship position measurements. These errors lead to errors in the calculated values of $\overline{U}$ and $\overline{V}$ and to corresponding errors in the mean Doppler correction, f_{SHIFT}, from equation (33). The ship spectra are also degraded in quality since the angle of the line-of-sight cells from the ship boresite is 42.5°.

For the July 1994 northern leg (Figure 18b), the line-of-sight ship spectra are of poor quality and there is little coincidence between the peak spectral pairs of the mirror-imaged ship spectra and the peak spectral pairs of the shore spectra. The poor quality of the ship spectra is probably due to the angle of the line-of-sight cells from the ship boresite being 45.1°, which is slightly beyond the 45° limitation of the OSCR system. This angular problem is exaggerated by the ±0.6° yaw which occurred during this leg.

For the July 1994 southern leg (Figure 18c), the peak spectral pairs of the mirror-imaged ship spectra and the peak spectral pairs of the shore spectra are virtually co-located, which is the expected result. The angle of the line-of-sight cells from the ship boresite is 12.3°. The ship spectra are of relatively good quality, though not of the same quality as the shore spectra.

Effects of GPS Errors on Extracted Radial Currents

The ship-based, Doppler corrected radial currents R_C extracted from OSCR data for the December 1993 northern leg, the July 1994 northern leg and the July 1994 southern leg are shown in Figures 19a, 19b and 19c, respectively. The radial currents are restricted to ranges between 1 and 5 km from the array and to angles between ±35° of the array boresite. There is a noticeable circulation or swirl, on the order of 30 to 50 cm/s, associated with the radial currents. This perceived circulation is due primarily to GPS errors. Suppose that the true mean ahead velocity $\overline{U}_T$ is given by $\overline{U}_T = \overline{U} + \delta\overline{U}$ where the velocity error $\delta\overline{U}$ is caused by GPS errors. Similarly, suppose that the true mean drift velocity $\overline{V}_T$ is given by $\overline{V}_T = \overline{V} + \delta\overline{V}$. Also assume that the velocity errors are proportional to the measured velocities; that is that
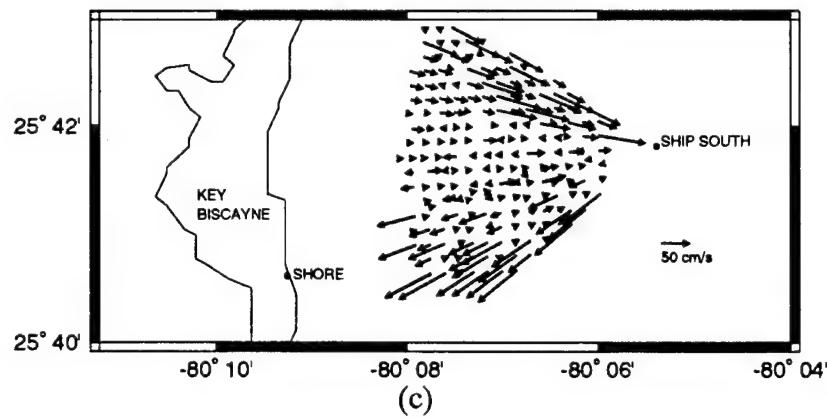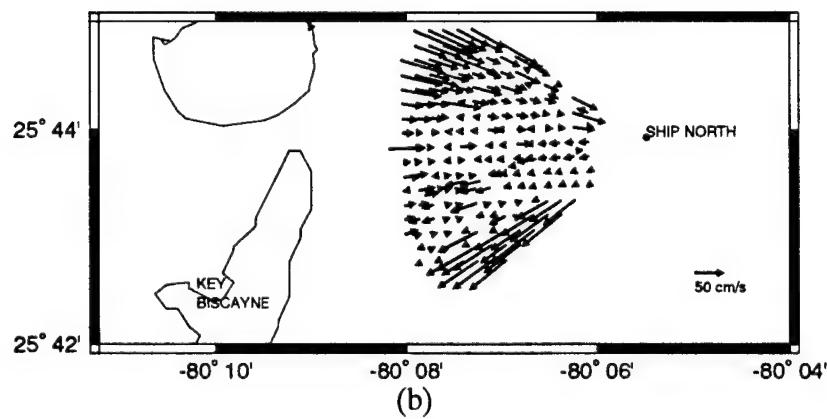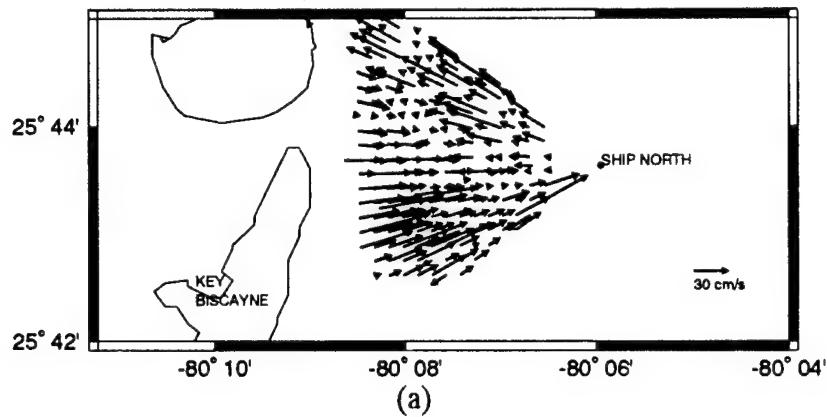
Figure 19. Doppler corrected radial currents. (a) December 1993 northern leg; (b) July 1994 northern leg; (c) July 1994 southern leg.

$\delta \overline{V}/\overline{V} = \pm \delta \overline{U}/\overline{U}$. Substituting these relations for $\overline{U}_T$, $\overline{V}_T$ and $\delta \overline{V}$ into equation (32), the relationship between the extracted radial current and the true radial current R_T is found as

$$R_C = R_T + \delta \overline{U}\left(\sin\theta \pm \frac{\overline{V}}{\overline{U}}\cos\theta\right) \tag{38}$$

For the three legs represented in Figure 19, $\overline{V} < \overline{U}$ (see Table 1) and the extracted radial currents consist dominantly of the true radial currents plus the circulation pattern $\delta \overline{U}\sin\theta$.

Since the pseudo-circulation pattern is defined mathematically by equation (38), it should be possible to develop algorithms to minimize GPS errors in the extracted radial currents. However, the development of such algorithms is beyond the scope of this work. It should be noted though that, since GPS errors are bounded, the influence of these errors on R_C decreases as R_C increases.

Vector Current Maps

The combination of the ship and shore-based radial currents to form a vector current map is contingent on three restricting factors. First, the ship-based cells must be within 1 to 5 km of the ship and within ±35° of the array boresite so that radial currents can be extracted with confidence from the ship-based spectra. Secondly, a ship-based and a shore-based cell must be within reasonable proximity to each other. Finally, the absolute angle subtended by the radials at the proximate cells must be greater than |30°| and less than |150°| so that a good vector current can be constructed from the two radial currents.

Several cell pairs having a separation of less than 115 m for the December 1993 northern leg are shown in Figure 20a. For clarity, not all of the selected cell pairs are depicted. For each selected pair, the latitudes and longitudes of the two cells are averaged, and both radials are assumed to have their origins at this new location, as shown in Figure 20b. The vector current is then calculated using equations (12) through (15). The final vector current map for the December 1993 northern leg is shown in Figure 20c. This methodology is used to generate all moving ship vector maps.

The December 1993 northern leg was conducted on December 10 at 1700 GMT. Based on tide tables, low tide in the inlet just north of Key Biscayne occurred at 1740 GMT. From previous investigations (Skop et al., 1994), an outflow from the inlet at 1700 GMT would be

34
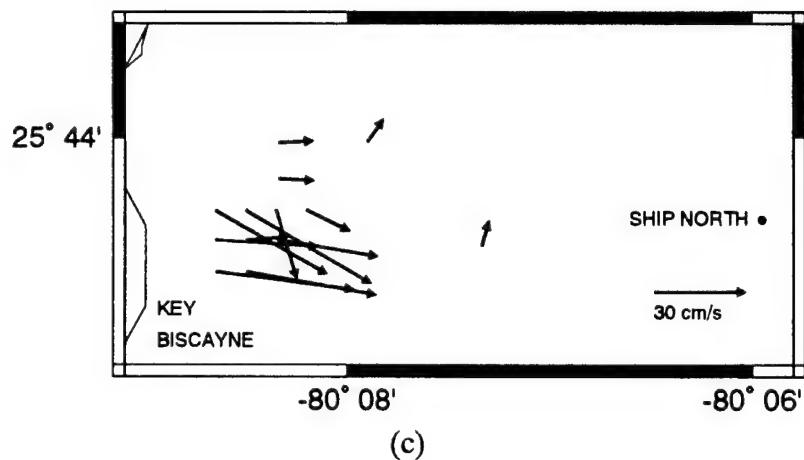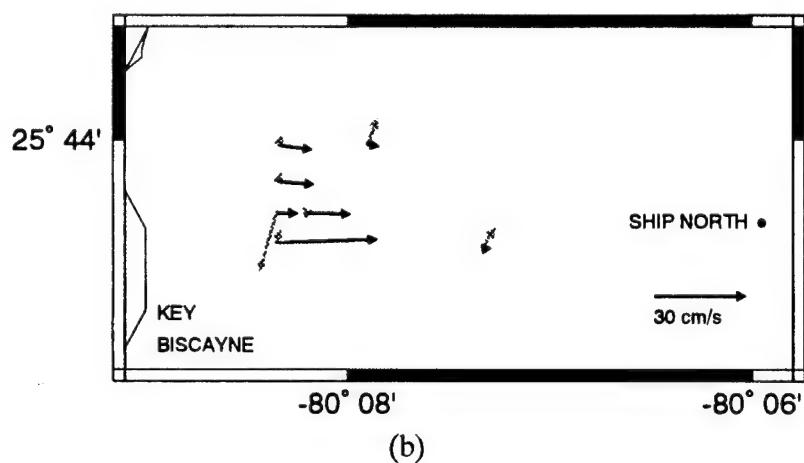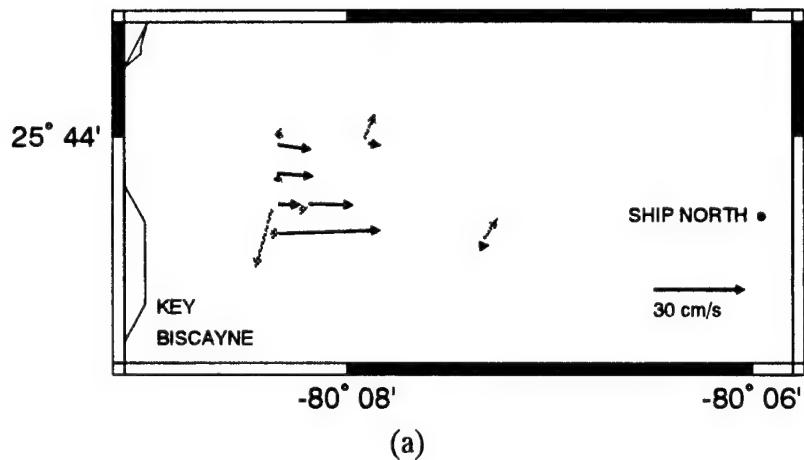
Figure 20. Generation of vector current map for the December 1993 northern leg. (a) Proximate cell pairs; (b) co-located cell pairs; (c) final vector map.

35
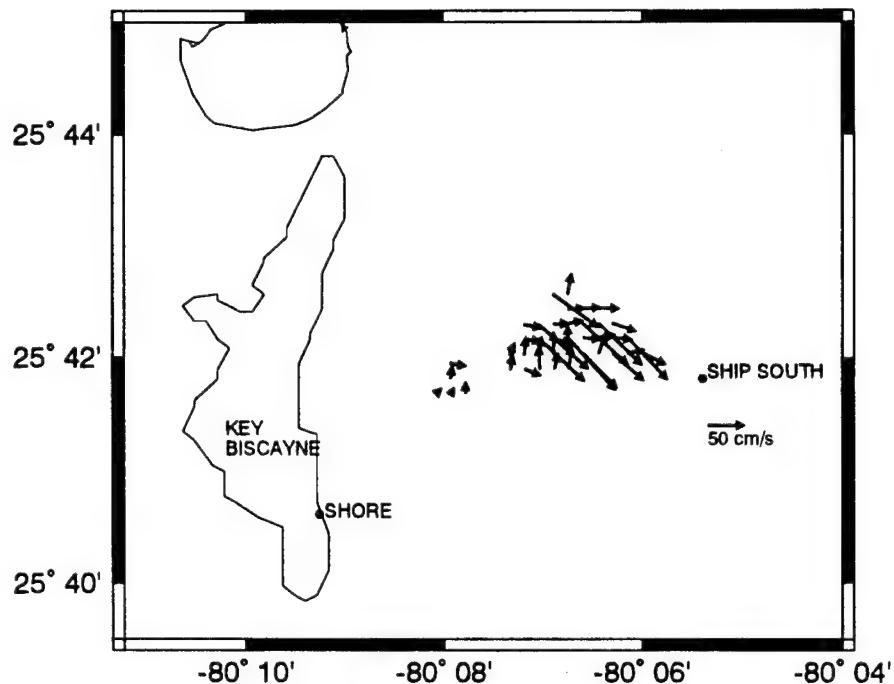
Figure 21. Vector current map for the July 1994 southern leg.

expected, as shown in Figure 20c. However, current magnitudes should be on the order of 15 to 20 cm/s, while those shown in the figure are on the order of 30 to 50 cm/s. This overestimation of the current magnitudes is attributable to the pseudo-circulation introduced by GPS errors, as can be seen by re-examining Figure 19a which shows a counterclockwise swirl of about 30 cm/s for this leg.

The vector current map for the July 1994 southern leg is shown in Figure 21. The proximity measure for the ship and shore-based cell pairs was taken as 115 m. The July 1994 southern leg was conducted on July 22 at 1830 GMT, which preceded a low tide in the inlet north of Key Biscayne by 1½ hours. Based on previous studies (Skop et al., 1994), a generally easterly flow of less then 10 cm/s would be expected in the area of coverage. The flow pattern and large current magnitudes on the order of 50 cm/s shown in Figure 21 are directly attributable to the pseudo-circulation introduced by GPS errors. This can be seen by re-examining Figure 19c which shows a clockwise swirl of about 50 cm/s for this leg.

From the results for the December 1993 northern leg and the July 1994 southern leg, it is apparent that algorithms to remove pseudo-currents due to GPS positioning errors must be

36

developed if low speed currents are to be measured accurately from a moving ship. Alternatively, highly precise differential or military GPS systems should be employed to determine mean ship velocities.

MOVING SHIP EXPERIMENT - OFFSHORE

Conduct of the Experiment

In July 1994, the COLUMBUS ISELIN made transects, twice, in a square pattern offshore of Key Biscayne and within the Florida Current. The weather during these experiments was characterized by winds of less than 7 m/s and light seas. The objective of these transects was to place a set of overlapping deep water grids of the OSCR footprint and to examine the possibility of generating the OSCR vector current maps from a single, moving platform. The OSCR transmit-receive cycles coincided with the ship at the central position of each of the square sides. The ship path and GMT times from immediately preceding to immediately following each data collection cycle are shown in Figures 22a and 22b, for the first and second square transects, respectively,.

Each square transect was initiated with a south to north pass (legs 1 and 5), followed by a west to east pass (legs 2 and 6) and a north to south pass (legs 3 and 7), and concluded by an east to west pass (legs 4 and 8). The influence of the northerly flow of the Florida Current can be seen in Figures 22a and 22b through the northerly drift of the ship during the west to east and east to west passes.

Ship Motions

The mean ship velocities, $\overline{U}$ and $\overline{V}$, headings and heading variations for the offshore legs are summarized in Table 3. The mean velocities were obtained from the GPS readings, the heading from the ship compass readings, and the heading deviation from the continuous accelerometer readings. The mean ahead velocities $\overline{U}$ were all on the order of 1 m/s or less. The mean drift velocities $\overline{V}$ were small for the south to north and north to south passes (legs 1, 3, 5 and 7). For the west to east and east to west passes (legs 2, 4, 6 and 8), the absolute values of the mean drift velocities were on the order of 1.0 to 1.7 m/s due to the influence of the Florida
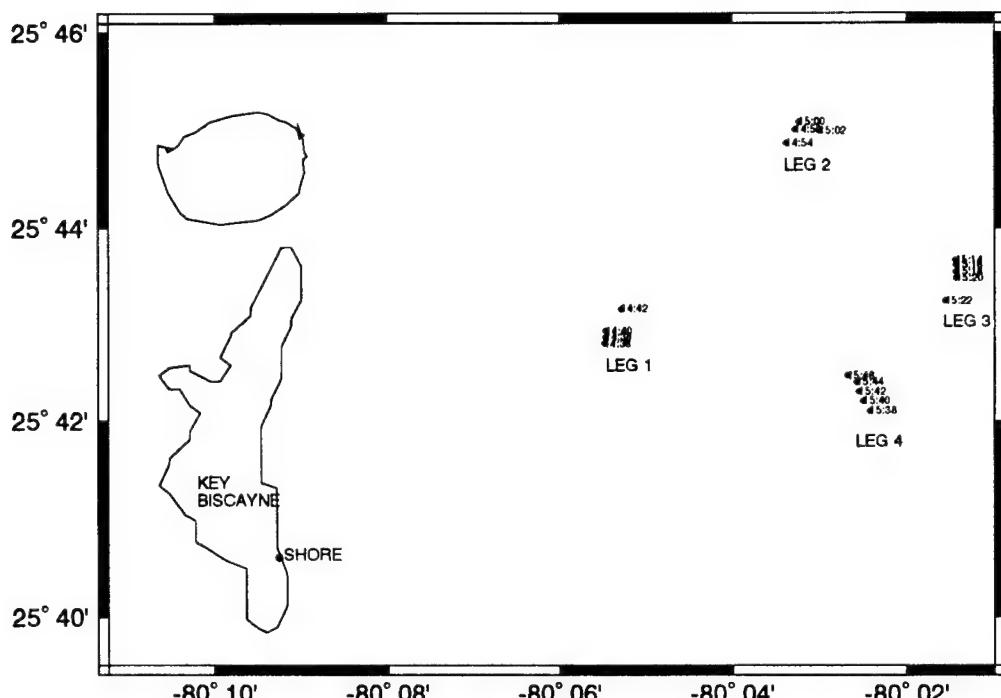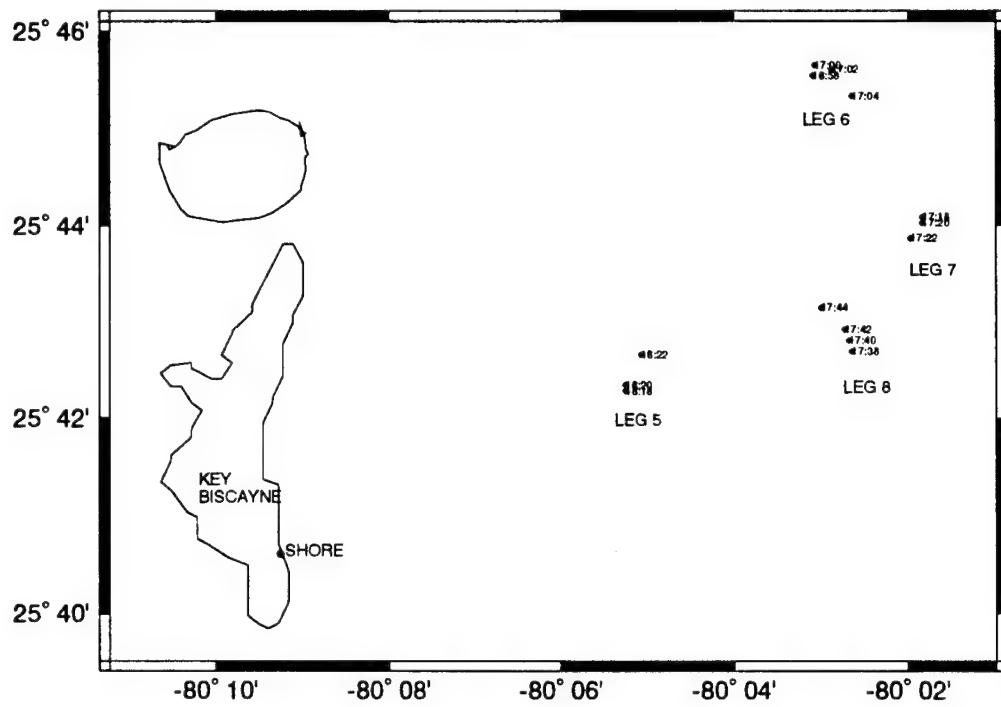
Figure 22. Ship trajectories for the July 1994 offshore moving ship experiment. (a) Square one, legs 1 through 4; (b) square two, legs 5 through 8.

Current. The heading variations for all eight legs were bounded by ±1.4°. The mean velocities and heading variations for the eight offshore legs were within satisfactory bounds for obtaining valid OSCR measurements from a moving ship.

The periodic ship motions recorded at the transmit antenna during the eight offshore legs are summarized in Table 4. Since the transmit antenna experienced the maximum motions of any of the antenna elements, the values of $(U'T)_{max}$ and $(V'T)_{max}$ represent the maximum effect of oscillatory ship motions on the ship-induced Doppler spectrum modulations as defined by equations (30) and (31). The maximum summed modulation value is given by $(VT)_{max} = (U'T)_{max} + (V'T)_{max}$. The largest value of $(VT)_{max}$ for the offshore legs was 1.01 m for leg 8. Transposing this value to Figure 5, the motion-induced sideband peaks during the offshore legs were at least 15 dB down from the expected Doppler peaks.

Spectral Returns

Doppler spectra received from cells along the boresite of the receive array are shown in Figures 23, 24, 25 and 26 as a function of increasing distance from the ship for legs 1, 2, 3 and 4, respectively, of the first square transect. The spectra for the second square transect are similar and are not presented. The expected 2 *FBG* separation and the selected peak spectral pairs are indicated in the figures. The quality of the spectra for legs 1, 2 and 4 (Figures 23, 24 and 26) is reasonably good, and clearly improved over the spectra obtained during the Key Biscayne passes. The peak pairs are easily discernable. For the leg 3 north to south pass (Figure 25), the quality of the spectra is poor and, in fact, of lesser quality than the Key Biscayne spectra. The reason for the poor quality of the spectra for the legs 3 and 7 north to south passes is unknown. The distinguishing contrast between these legs and all of the other legs is the large (on the order of 3 m/s) ship speed relative to water due to the northerly flow of the Florida Current.

Doppler spectra received from mid-range cells are shown in Figures 27, 28 and 29 as a function of the cell angle θ, ranging from +45° to -45° from the boresite, for legs 1, 2 and 4, respectively, of the first square pattern. The mid-range spectra for leg 3 are not included, as the spectra are of poor quality. However, the quality of the mid-range spectra for legs 1, 2 and 4 is good with easily discernable peak pairs even out to the extreme ±45° angles of the system.

The poor quality of the spectra from legs 3 and 7 and the relative orientations of the ship

Table 3. Mean velocities, headings, and heading variations for the offshore legs.

Offshore	$\overline{U}$ (ms⁻¹)	$\overline{V}$ (ms⁻¹)	Heading (deg)	Yaw (deg)
Leg 1	0.99	0.11	356.1	±0.6
Leg 2	0.93	-1.02	78.3	±0.9
Leg 3	1.04	-0.03	179.9	±1.2
Leg 4	1.15	1.45	273.5	±1.2
Leg 5	0.99	0.09	355.0	±1.4
Leg 6	0.23	-1.68	89.5	±1.4
Leg 7	0.95	0.02	176.7	±1.1
Leg 8	0.19	1.72	271.5	±1.2

Table 4. Periodic ship motions for the offshore legs.

Offshore	U' (ms⁻¹)	V' (ms⁻¹)	$(U'T)_{max}$ (m)	$(V'T)_{max}$ (m)
Leg 1	±0.5	±0.6	0.32	0.35
Leg 2	±0.5	±0.6	0.26	0.22
Leg 3	±0.6	±0.8	0.25	0.26
Leg 4	±0.8	±0.8	0.44	0.47
Leg 5	±0.3	±0.9	0.30	0.41
Leg 6	±0.5	±0.6	0.20	0.25
Leg 7	±0.4	±0.6	0.26	0.44
Leg 8	±0.7	±0.9	0.43	0.58
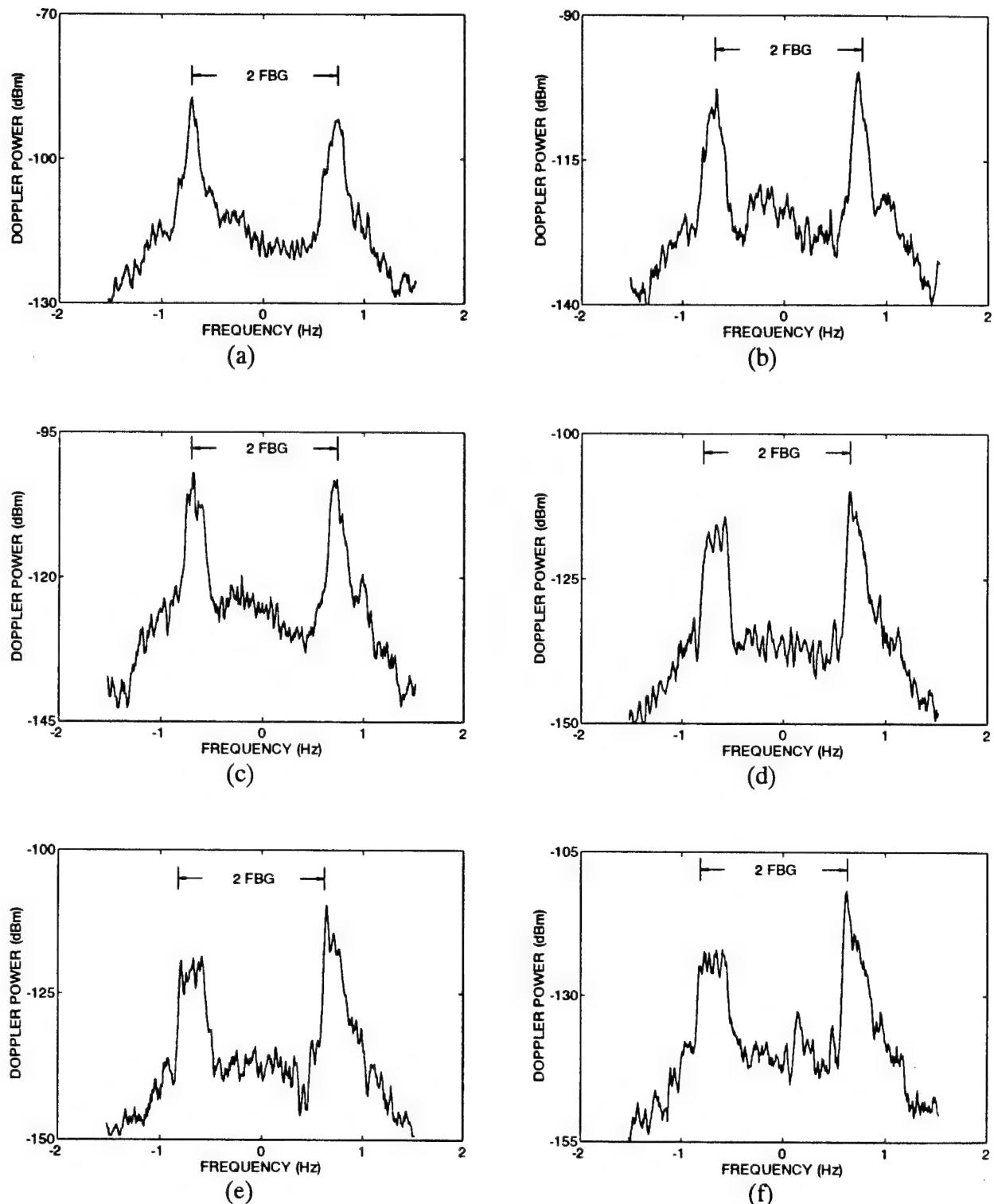
Figure 23. Doppler spectra from cells along boresite versus increasing distance from ship during the July 1994 offshore leg 1. (a) 839 m; (b) 2198 m; (c) 2475 m; (d) 4136 m; (e) 4414 m; (f) 4969 m.

42
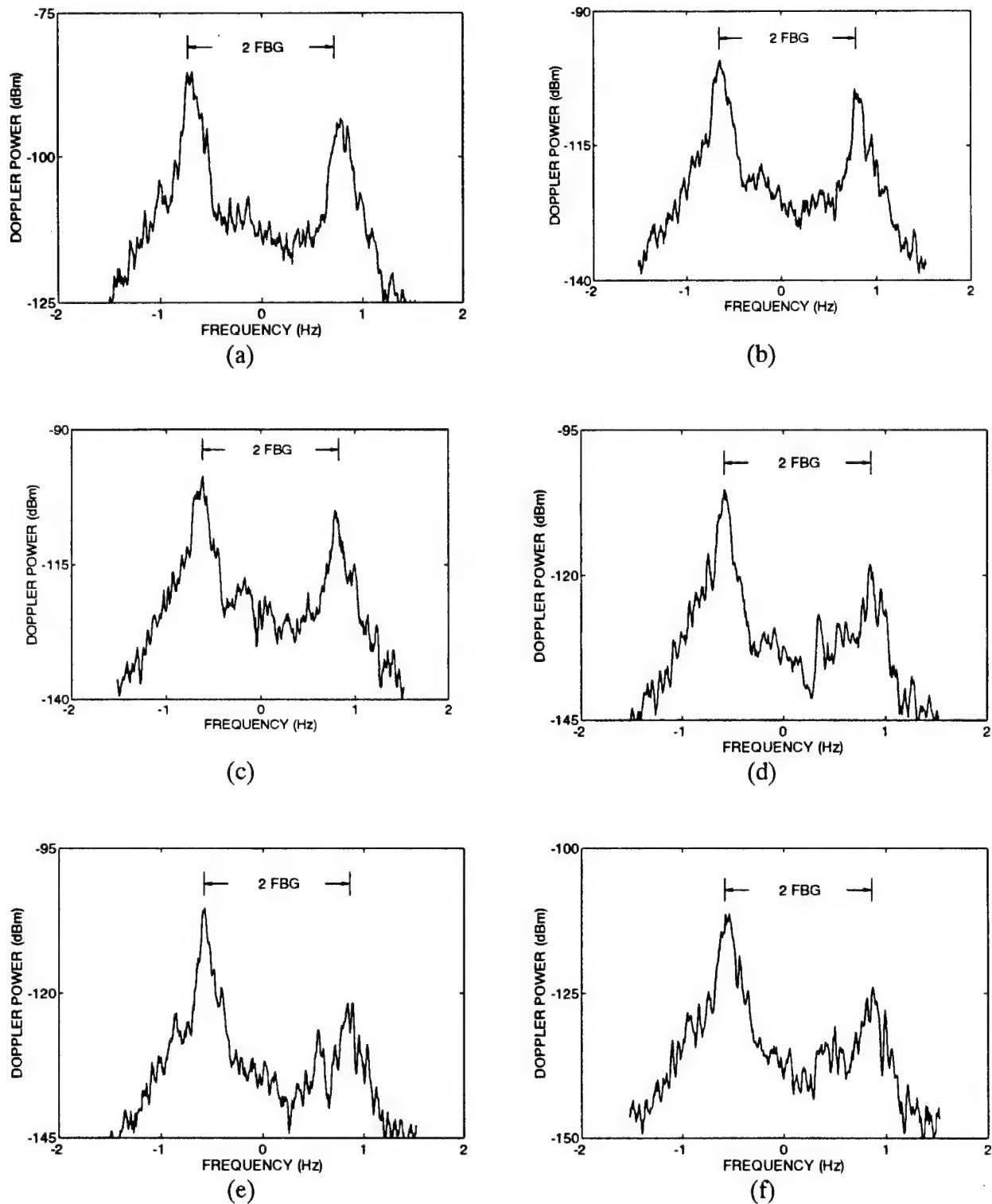
Figure 24. Doppler spectra from cells along boresite versus increasing distance from ship during the July 1994 offshore leg 2. (a) 839 m; (b) 2198 m; (c) 2475 m; (d) 4136 m; (e) 4414 m; (f) 4969 m.

43
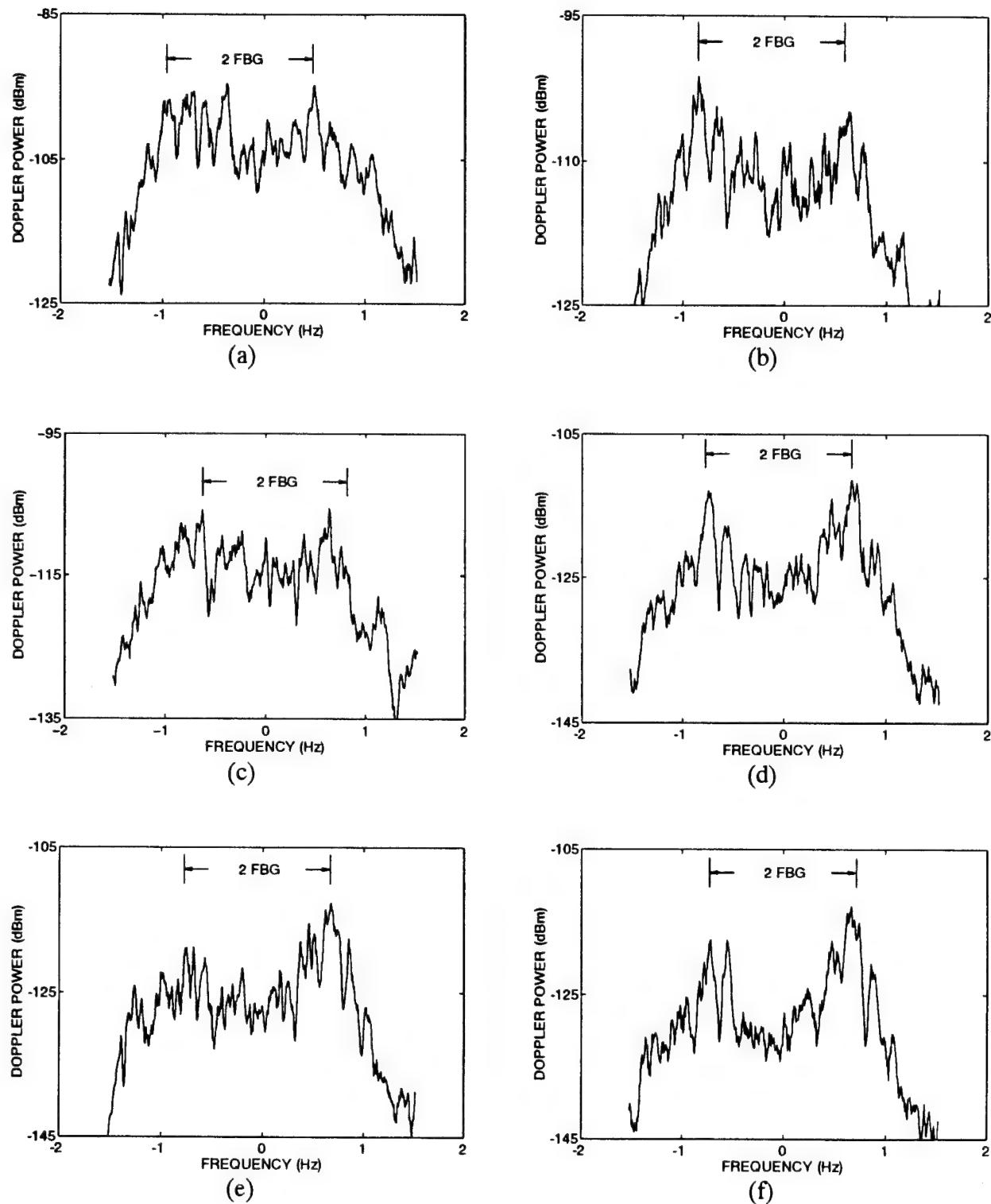
Figure 25. Doppler spectra from cells along boresite versus increasing distance from ship during the July 1994 offshore leg 3. (a) 839 m; (b) 2198 m; (c) 2475 m; (d) 4136 m; (e) 4414 m; (f) 4969 m.

44
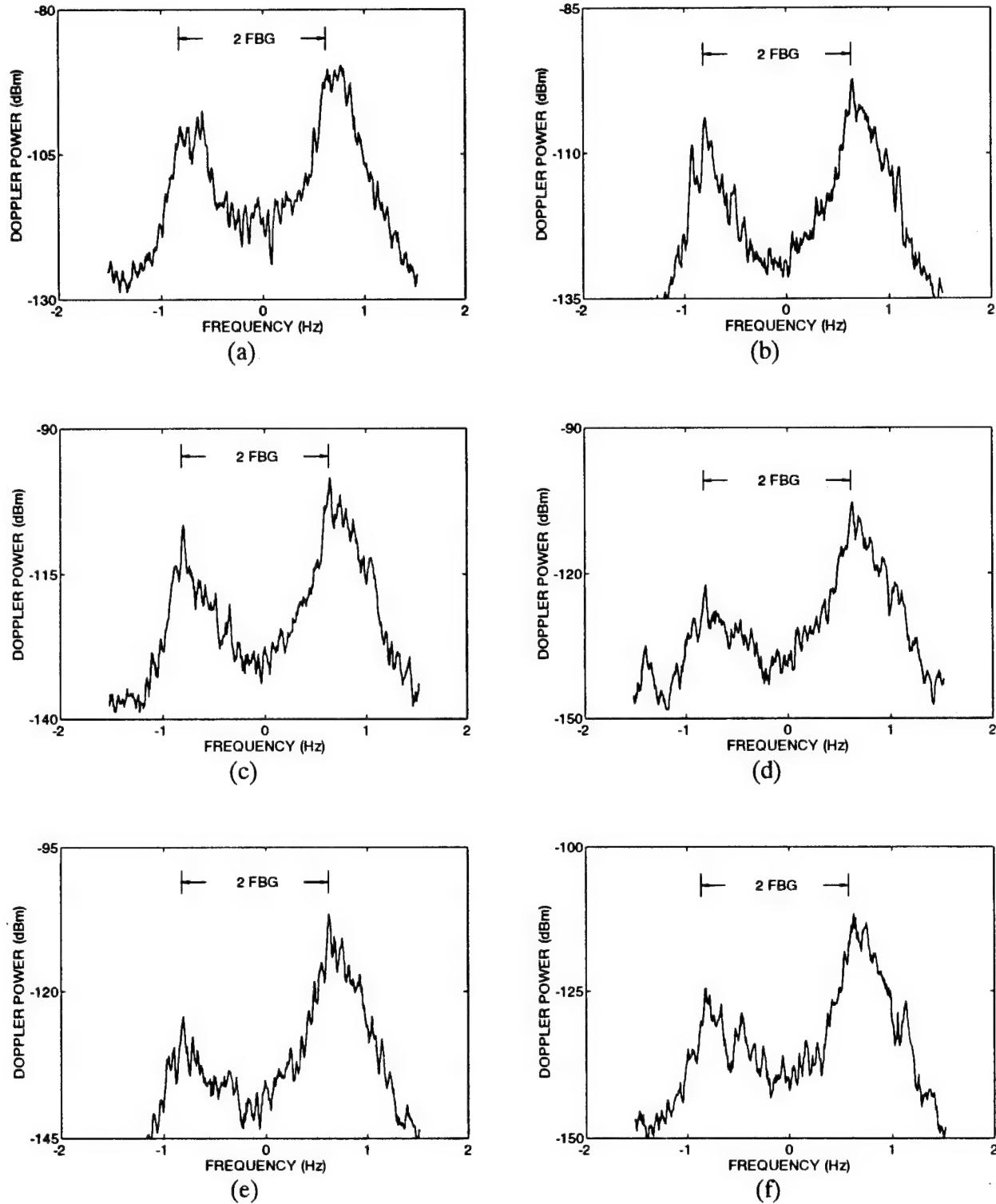
Figure 26. Doppler spectra from cells along boresite versus increasing distance from ship during the July 1994 offshore leg 4. (a) 839 m; (b) 2198 m; (c) 2475 m; (d) 4136 m; (e) 4414 m; (f) 4969 m.

45
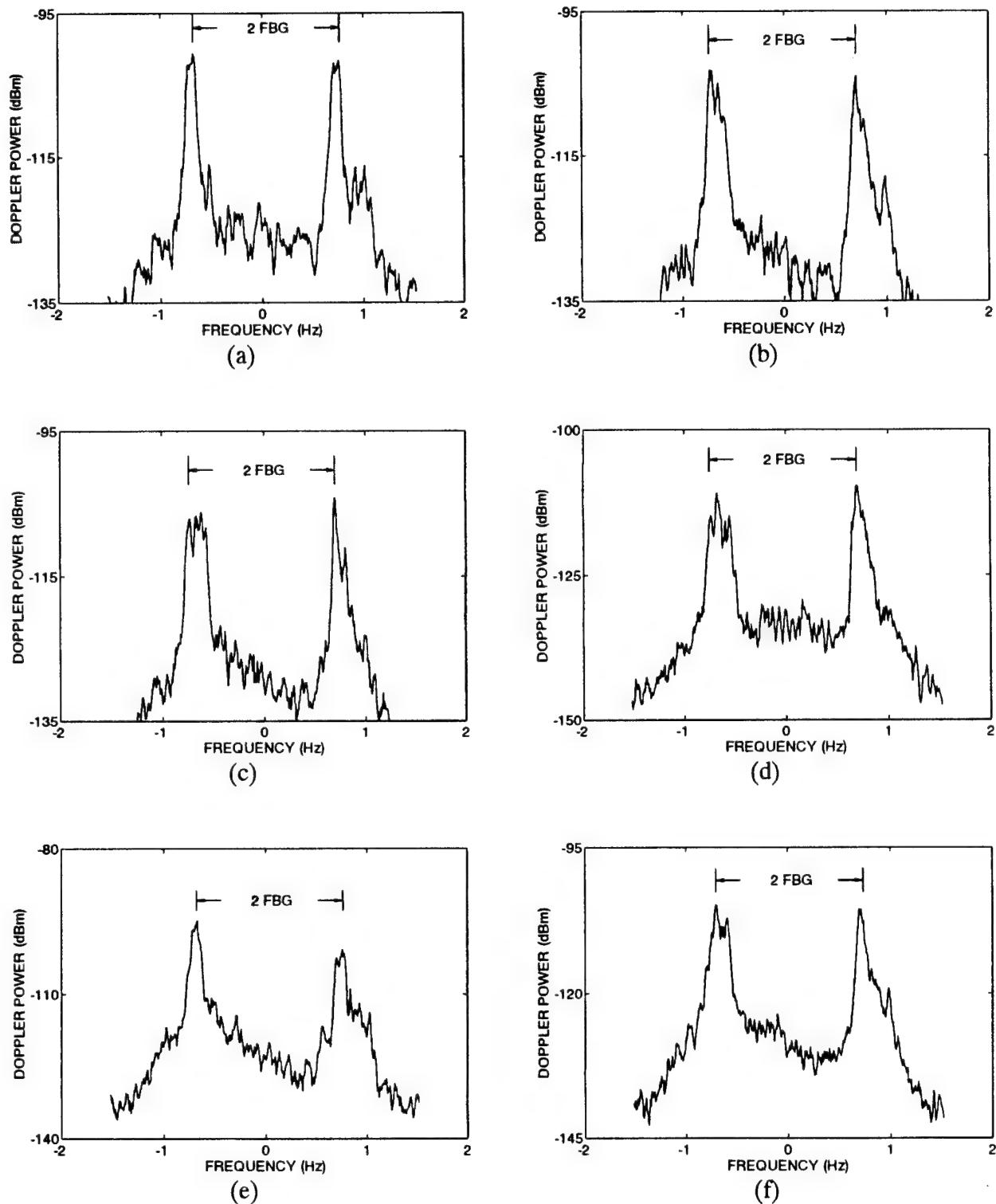
Figure 27. Doppler spectra from mid-range cells, 3.5 to 4.0 km, versus cell angle from the boresite for the July 1994 offshore leg 1. (a) 45°; (b) 35°; (c) 25°; (d) -25°; (e) -35°; (f) -45°.
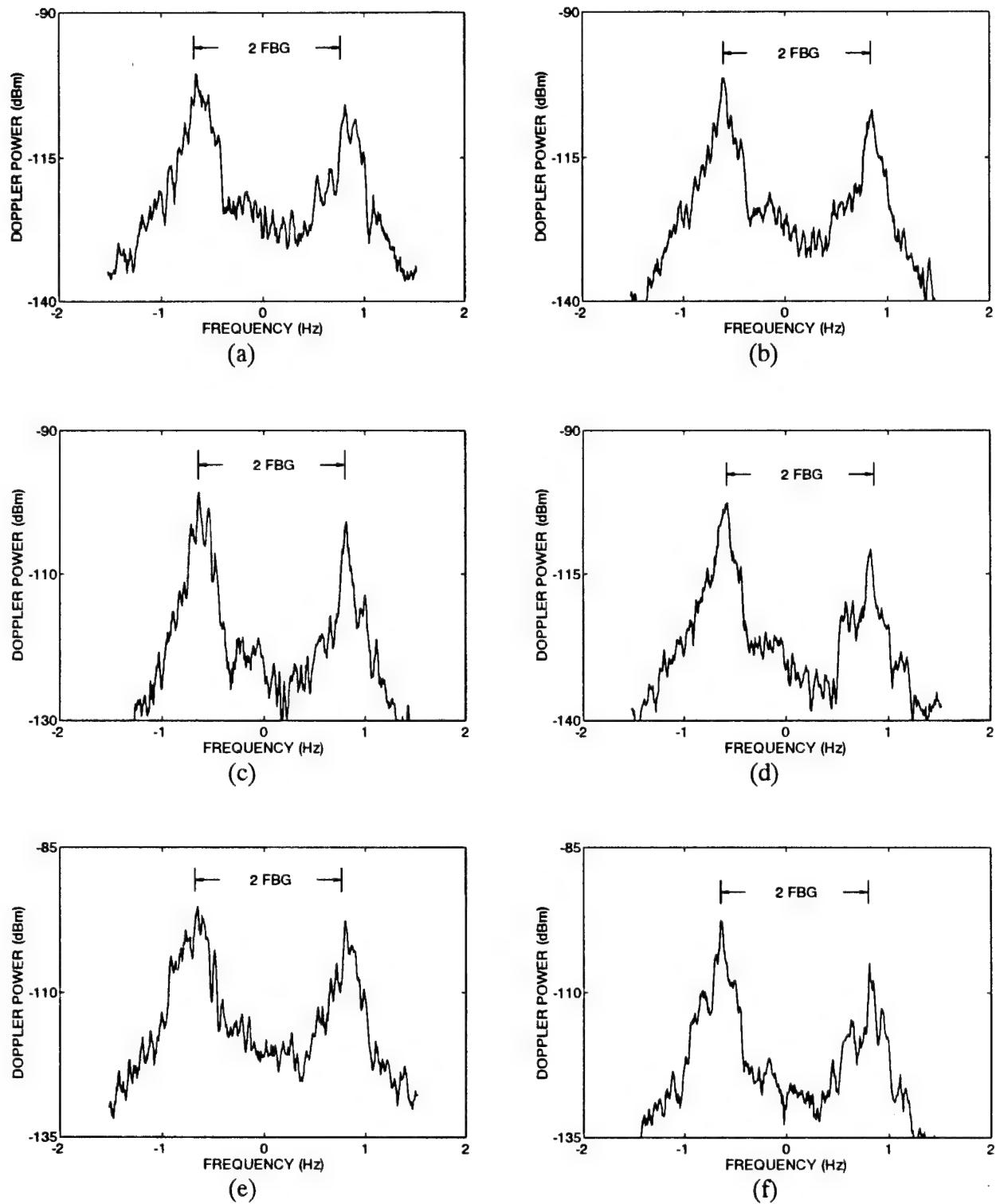
Figure 28. Doppler spectra from mid-range cells, 3.5 to 4.0 km, versus cell angle from the boresite for the July 1994 offshore leg 2. (a) 45°; (b) 35°; (c) 25°; (d) -25°; (e) -35°; (f) -45°.
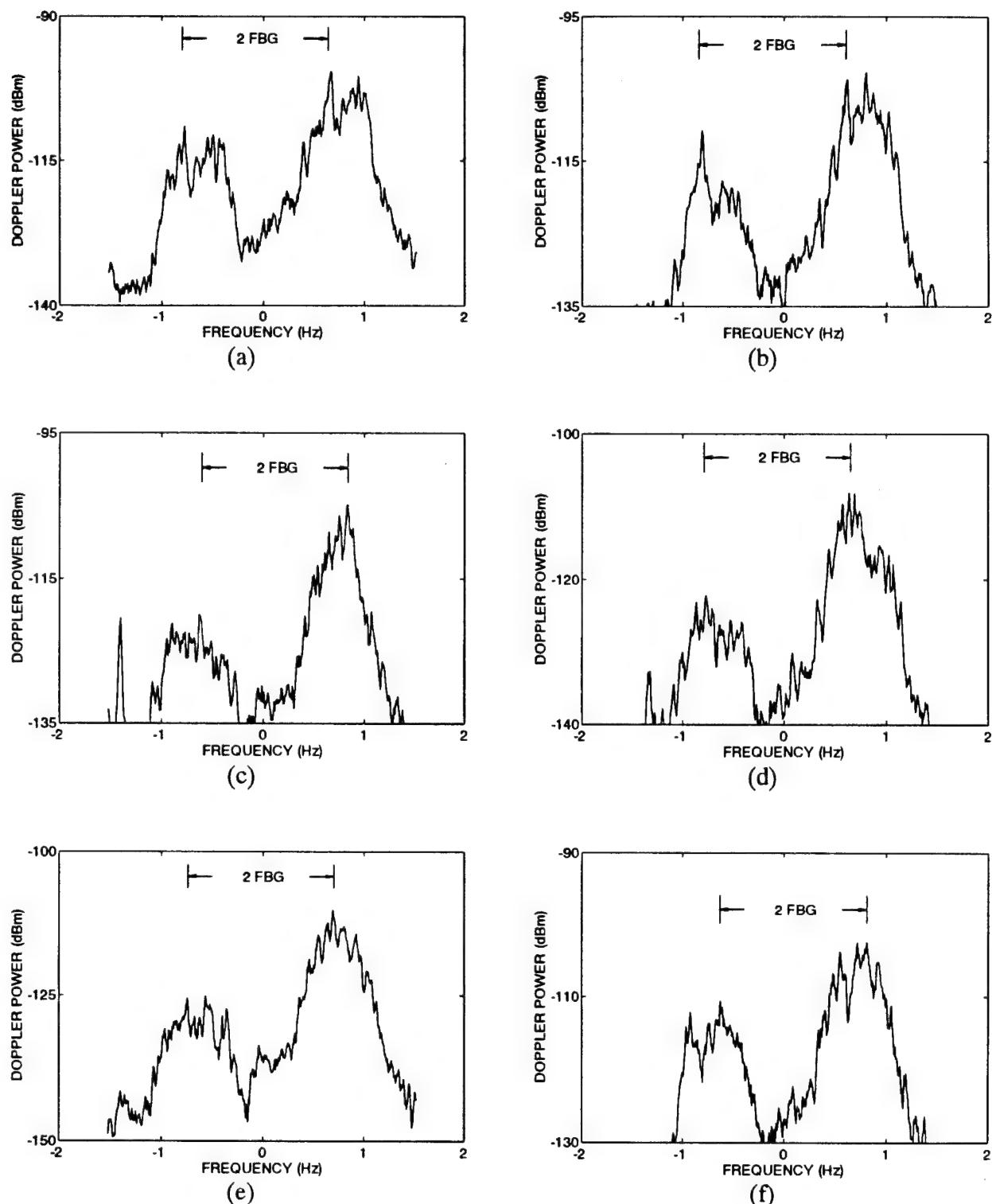
Figure 29. Doppler spectra from mid-range cells, 3.5 to 4.0 km, versus cell angle from the boresite for the July 1994 offshore leg 4. (a) 45°; (b) 35°; (c) 25°; (d) -25°; (e) -35°; (f) -45°.

48
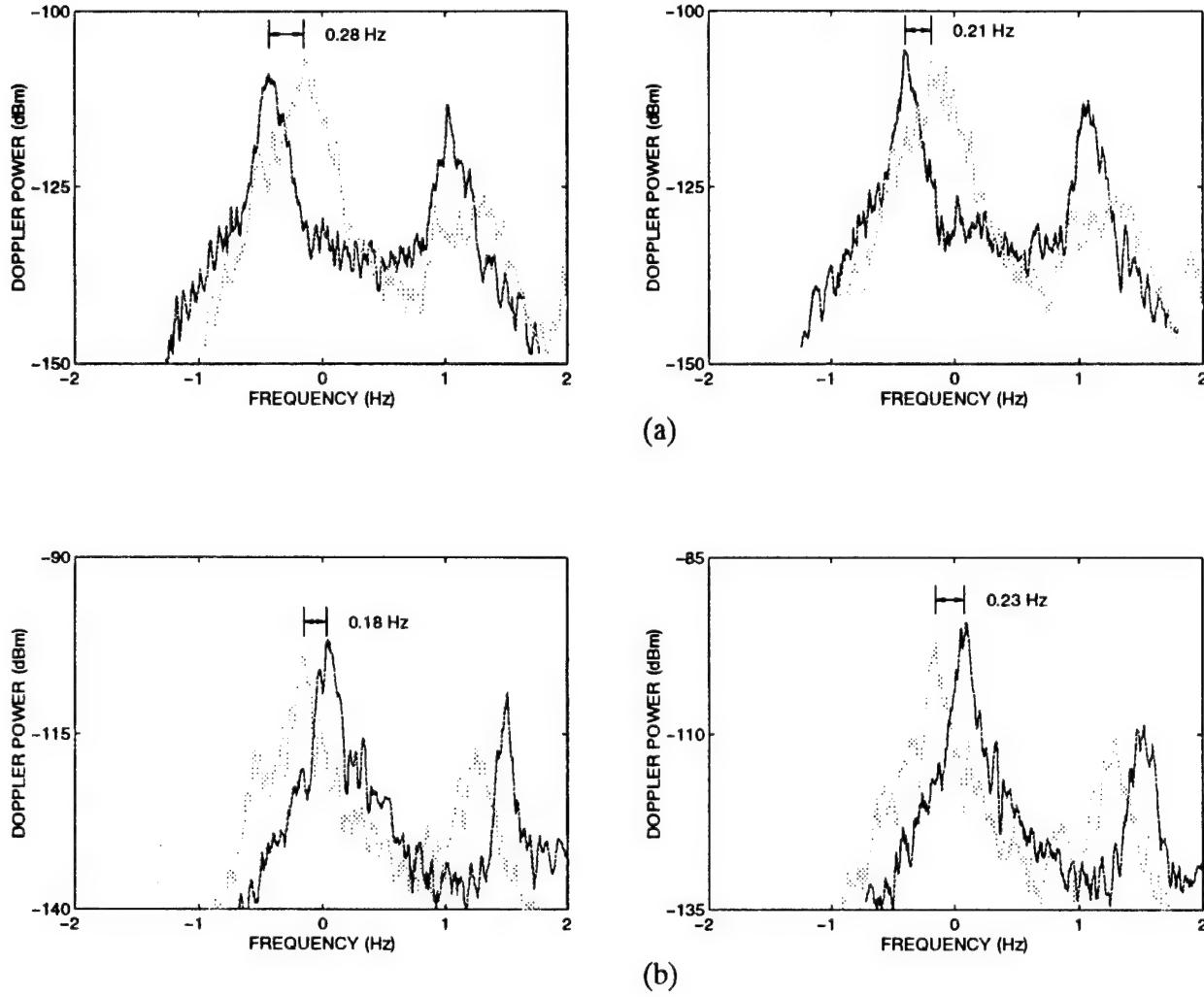
Figure 30. Comparisons of leg to leg, frequency corrected line-of-sight spectra. The frequency differences between the main peaks of the compared spectra are indicated. (a) From legs 2 and 4; (b) from legs 6 and 8.

between other legs restrict comparisons of the spectral returns from common cells lying along the line-of-sight between any two transects to legs 2 and 4, which are separated by 40 minutes in time, and legs 6 and 8, which are also separated by 40 minutes in time. The common cell spectral comparisons for legs 2 and 4 and legs 6 and 8 are shown in Figures 30a and 30b, respectively. The spectra have all been frequency shifted, as given by equation (33), to correct for mean ship motions. The spectra for legs 4 and 8 have then been reversed and overlaid on the corresponding spectra for legs 2 and 6. The cells compared are within 100 m of each other

49

and within 75 m of the line-of-sight. The angles of the line-of-sight cells from the ship boresite are 0.3°, 11.1°, 8.0° and 10.0° for legs 2, 4, 6 and 8, respectively.

As seen in Figure 30a, the mirror-imaged peak spectral pairs for leg 4 and the peak spectral pairs for leg 2 are displaced from one another. Similarly, as seen in Figure 30b, the mirror-imaged peak spectral pairs for leg 8 and the peak spectral pairs for leg 6 are displaced from one another. Assuming that the Florida Current flow pattern remains constant over the 40 minutes between legs 2 and 4 and over the 40 minutes between legs 6 and 8, the peak pair displacement is most likely due to GPS errors in ship position, from which $\bar{U}$ and $\bar{V}$ and, subsequently, f_{SHIFT} are determined. The offset between peak spectral pairs is also indicated in Figures 30a and 30b. For legs 2 and 4, this offset averages approximately 0.25 Hz corresponding, from equation (9), to a difference of 75 cm/s between the radial currents calculated at the common line-of-sight cells during leg 2 and those calculated during leg 4. For legs 6 and 8, the offset averages approximately 0.21 Hz which corresponds to a difference of 63 cm/s between the radial currents calculated at the common line-of-sight cells during leg 6 and those calculated during leg 8.

Vector Current Maps

The vector current map constructed from legs 1 and 2 is shown in Figure 31a. The cell pairs selected for the construction of the vector currents are within 75 m of each other. The vector current map constructed from legs 5 and 6 is shown in Figure 31b. Again, the cell pairs selected are within 75 m of each other. For each of the four legs, the cells used are within 1 to 6 km of the ship and within ±35° of the array boresite. Legs 1 and 2 are separated by 20 minutes in time while legs 5 and 6 are separated by 40 minutes in time.

A northerly surface current on the order of 175 cm/s was found from the data. For the vector current map constructed from legs 1 and 2 (Figure 31a), the mean value of the current over the OSCR grid is 163 cm/s with a standard deviation of 20 cm/s. The mean direction (bearing from north) of the flow is 1° with a standard deviation of 10°. For the vector current map constructed from legs 5 and 6 (Figure 31b), the mean value of the current over the OSCR grid is 177 cm/s with a standard deviation of 24 cm/s. The mean direction of the flow is 352° with a standard deviation of 8°. The mean values of the current magnitude and direction are
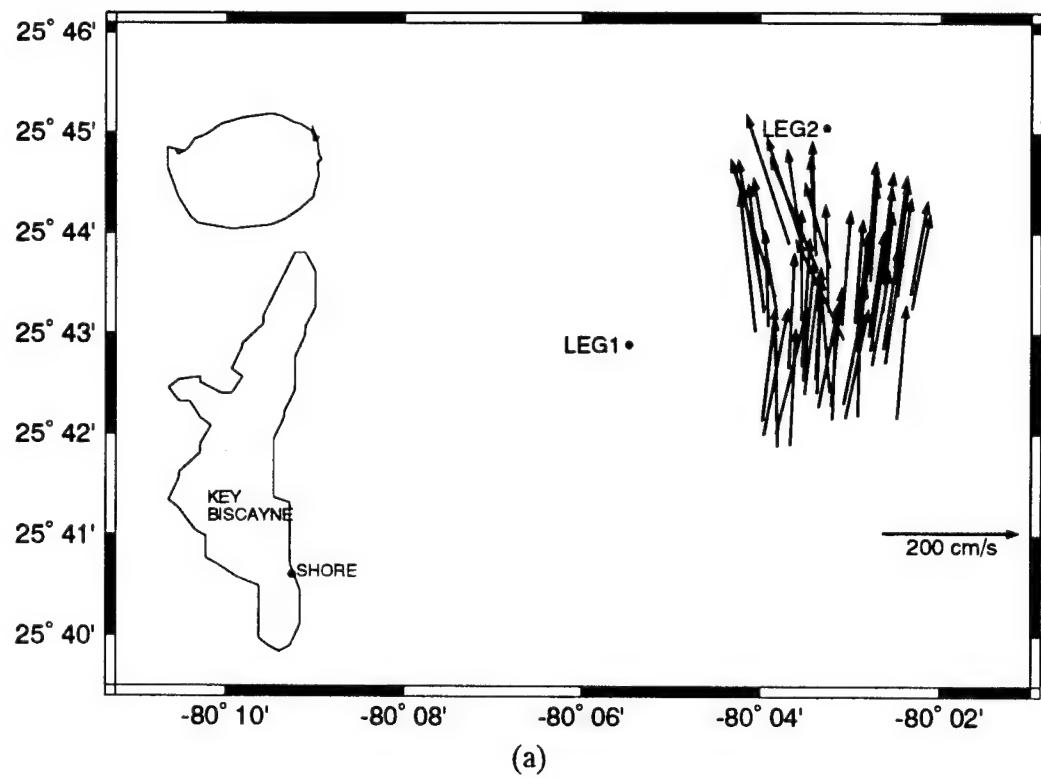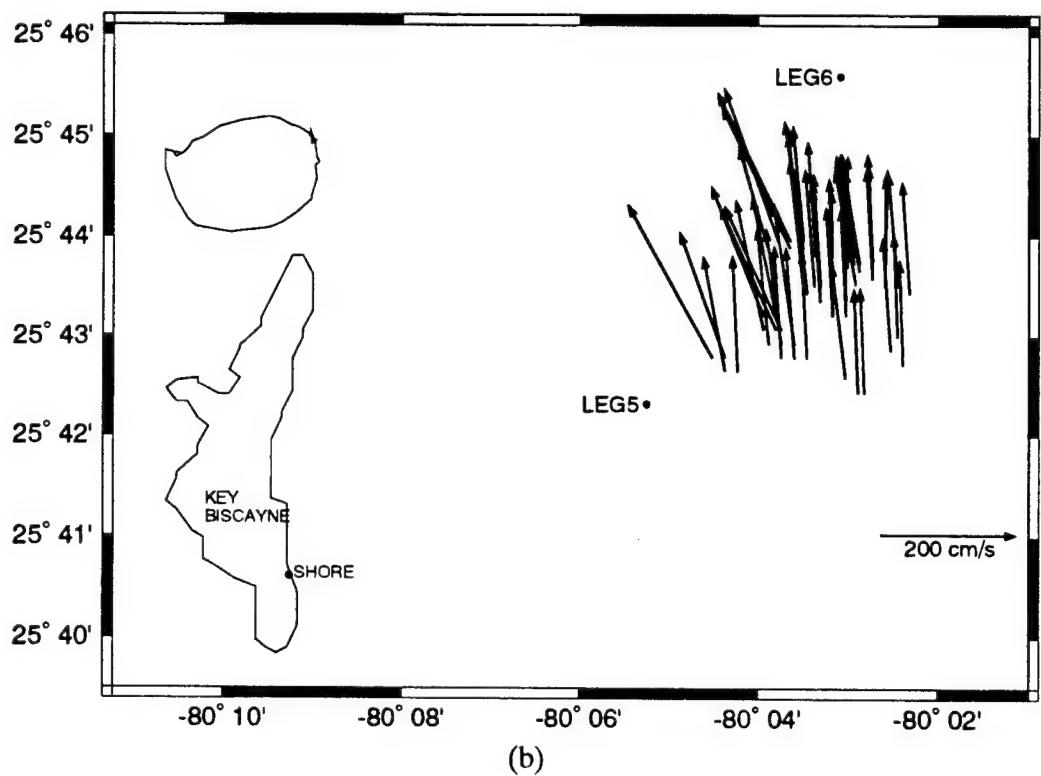
Figure 31. Vector current maps of the Florida Current on July 22, 1994. (a) From legs 1 and 2 at 1500 GMT; (b) from legs 5 and 6 at 1700 GMT.

consistent with the values measured in the Florida Current by Leaman et al. (1987). These results demonstrate the feasibility of generating vector current maps from a single, moving platform using an OSCR type system.

CONCLUSIONS

The nearshore and offshore experiments of December 1993 and July 1994 have demonstrated the capability of a ship-based OSCR system to obtain Doppler spectra of sufficient integrity for subsequent analysis of ocean surface currents. The OSCR system, although designed specifically for shore-based use, is adaptable to shipboard operation. The overriding inaccuracies in the calculated currents were uncertainties in the ship speed due to GPS errors in the determination of ship position. These uncertainties lead to inaccuracies in the removal of the ship-induced Doppler from the measured currents. Two possible methods of correcting for these inaccuracies have been discussed. First, GPS precision on the order of 1 m or less can be obtained by using differential or military GPS. This precision would reduce the uncertainties in ship speed to 2 cm/s or less. Second, algorithms can be derived to minimize the pseudo-circulation pattern due to GPS errors, as described in equation (38). The implementation of both methods would enable small currents to be mapped with a high degree of confidence.

The offshore north to south legs showed a considerable decrease in spectral quality as compared to the other nearshore and offshore legs. The reason for this decrease in spectral quality is unknown; the only apparent difference between these legs and the other legs being increased over-water speeds in the offshore north to south transects due to the northerly flow of the Florida Current. That the contamination of the spectra from the offshore north to south transects could be due to ship operating parameters is another possibility.

The vector current maps for the offshore square runs show the feasibility of utilizing a single, high frequency ground wave radar system from a moving platform for recording ocean surface currents. Even with a shore-based specific radar, the speed and direction of the Florida Current agrees well with the expected values. The OSCR system performance is best when the ship is moving at a slow ahead speed, but of sufficient value to enable accurate heading control.

Meriting additional investigation is the system response under a variety of sea conditions and ship speeds. Further development of a similar system, designed explicitly for ship-based

operation, is possible and should be considered for deep water and shallow water applications.

ACKNOWLEDGMENTS

REFERENCES

Barrick, D.E., 1972. First-order theory and analysis of MF/HF/VHF scatter from the sea. IEEE Trans. Antennas Propagat., AP-20, 2-10.

Brigham, E.O., 1974. The Fast Fourier Transform. Prentice-Hall, Englewood Cliffs, NJ.

Crombie, D.D., 1955. Doppler spectrum of sea echo at 13.56 Mc/s. Nature, 175, 681-682.

Leaman, K.D., R.L. Molinari and P.S. Vertes, 1987. Structure and variability of the Florida Current at 27°N: April 1982-July 1984. J. Phys. Oceanogr., 17, 565-583.

Oppenheim, A.V., A.S. Willsky and I.T. Young, 1983. Signals and Systems. Prentice-Hall, Englewood Cliffs, NJ.

Prandle, D., 1987. The fine-structure of nearshore tidal and residual circulations revealed by HF radar surface current measurements. J. Phys. Oceanogr., 17, 231-245.

Schott, F., A.S. Frisch, K. Leaman, G. Samuels and I.P. Fotiro, 1986. High-frequency Doppler radar measurements of the Florida Current in summer 1983. J. Geophys. Res., 90, 9006-9016.

Shay, L.K., H.C. Graber, D.B. Ross, L. Chemi, N. Peters, J. Hargrove, R. Vakkayil and L Chamberlain, 1993. Measurements of ocean surface currents using an HF radar during HIRES-2. RSMAS Technical Report 93-007.

Skop, R.A., D.B. Ross, N.J. Peters and L. Chamberlain, 1994. Measurements of coastal currents using a ship-based VHF radar system. RSMAS Technical Report 94-001.

Stewart, R.H. and J.W. Joy, 1974. HF radio measurements of surface currents. Deep Sea Res., 21, 1039-1049.